Scientific Data

https://doi.org/10.1038/s41597-026-07959-w

Article in Press

MRBA60: Long-term consistent global burned area dataset from Sentinel-3 and MODIS products

Received: 14 January 2026

Accepted: 20 July 2026

Published online: 25 July 2026

Cite this article as: Torres-Vázquez, M.&., Segura-Garcia, C., Turco, M. *et al.* MRBA60: Long-term consistent global burned area dataset from Sentinel-3 and MODIS products. *Sci Data* (2026). https://doi.org/10.1038/s41597-026-07959-w

Miguel Ángel Torres-Vázquez, Carlota Segura-Garcia, Marco Turco, Amin Khairoun, M. Lucrecia Pettinari, Erika Solano-Romero, Mariano García, Patricia Oliva, Matthew W. Jones & Emilio Chuvieco

MRBA60: Long-term consistent global burned area dataset from Sentinel-3 and MODIS products

Miguel Ángel Torres-Vázquez[1]***,** Carlota Segura-Garcia[2], Marco Turco[3], Amin Khairoun[1], M. Lucrecia Pettinari[1], Erika Solano-Romero[1], Mariano García[1], Patricia Oliva[1], Matthew W. Jones[2], Emilio Chuvieco[1]

1. Universidad de Alcalá, Environmental Remote Sensing Research Group, Department of Geology, Geography and the Environment, Alcalá de Henares, Spain
2. Tyndall Centre for Climate Change Research, School of Environmental Sciences, University of East Anglia (UEA), Norwich, UK.
3. Regional Atmospheric Modelling (MAR) Group, Department of Physics, Regional Campus of International Excellence Campus Mare Nostrum (CEIR), University of Murcia, Murcia, Spain

Corresponding author (*): miguela.torres@uah.es

Abstract

As the MODIS mission nears its end, ensuring continuity between legacy burned area (BA) records and products from newer sensors is essential for climate applications. Here we present the *Medium Resolution Burned Area Grid product version 6.0* (*MRBA60*), a continuous global BA time series for 2003-present, assembled on a monthly 0.25° grid by combining two components archived in separate Centre for Environmental Data Analysis (CEDA) entries: the harmonised historical MRBA60H component for 2003-2018 and the FireCCIS311 grid product from 2019 onwards. For 2003-2018, we train biome- and season-specific Random Forest models on the overlap period (2019-2024) between FireCCI51 (based on MODIS 250 m data) and FireCCIS311 (derived from Sentinel-3 SYN 300 m data) BA using auxiliary predictors (active fires, fire radiative power, climate, and vegetation indices), followed by a quantile-mapping bias correction to fit the FireCCIS311 BA distribution better. MRBA60 increases global BA relative to FireCCI51 by ~1.1 Mkm² of additional BA per year while preserving the reported decline in BA over the past two decades. Validation against Landsat-based and regional high-resolution products generally shows improved agreement compared with FireCCI51 and NASA's MCD64A1.

Background & Summary

Burned Area (BA) monitoring is crucial to understanding trends, drivers, and impacts of fire on the Earth system[1,2]. Fires have long contributed to ecological and cultural processes[3], but growing human exposure in fire-prone regions and climate-driven increases in extreme fire weather conditions are making their consequences increasingly severe[4–10]. In addition to contributing to the understanding of fire effects, BA monitoring is key to improving fire occurrence predictions at different temporal scales[11–13], calibrating and validating fire spread simulation models[14,15], and identifying the main drivers (climatic, ecological, or anthropogenic) that explain the variability and evolution of fire regimes[16–19].

Within the Climate Change Initiative (CCI) of the European Space Agency (ESA), the FireCCI project has developed several algorithms for BA detection using different satellite sensors, generating global and regional products with varying temporal coverage and spatial resolution. The first product, FireCCI41 (2005-2011), was based on images from the MERIS sensor, guided by the Moderate-Resolution Imaging Spectroradiometer (MODIS) Active Fire (AF) product[20]. The original algorithm was adapted to 250-m MODIS red and near-infrared reflectance data, producing the FireCCI50 dataset[21,22], extending the time series to the period 2001-2016, again guided by MODIS AF. Although FireCCI50 improved the accuracy of FireCCI41 (with a 13% reduction in commission error and a 10% reduction in omission error)[23], it still presented limitations. Among the most notable were edge effects in fires located near tile boundaries, low sensitivity to small or low-intensity fires, and an overestimation of BA due to the expansion of burned pixels. To address these shortcomings, a new version of the algorithm was developed, producing the FireCCI51 product, which extended the time series to 2022 and improved both thematic accuracy and temporal dating[23]. The FireCCI51 datasets include monthly pixel (250 m) and grid (0.25º) products. In addition to BA data, the products incorporate different auxiliary layers (uncertainty, land cover, observed, and burnable area). These datasets are archived and distributed via the Centre for Environmental Data Analysis (CEDA) catalogue (https://catalogue.ceda.ac.uk/uuid/3628cb2fdba443588155e15dee8e5352/).

After more than two decades of global observations, the MODIS mission is approaching the end of its operational life, posing a challenge to the continuity of FireCCI51 and other BA datasets[24]. In anticipation of this, and considering the new possibilities opened by the Sentinel-3 missions, the FireCCI team developed a new BA product called FireCCIS310[24], based on the Sentinel-3 Synergy (SYN) reflectance, that resamples the 500 m surface reflectance information from the Sea and Land Surface Temperature Radiometer (SLSTR) into the 300 m resolution Ocean and Land Colour Instrument (OLCI) grid[25], together with 375 m resolution AF detections from the Visible Infrared Imaging Radiometer Suite (VIIRS)[26] onboard the Suomi National Polar-orbiting Partnership (S-NPP) satellite. This new product demonstrated greater sensitivity for detecting small and short-duration fires, estimating ~27% more BA than FireCCI51 during 2019 (the year used to develop the algorithm)[24]. However, FireCCIS310 showed a small inconsistency in the assignment of burning dates, which was corrected in the recent version of the algorithm, called FireCCIS311[27], which spans from 2019 to the present. Following refs[28,29], validation results showed improved performance of this product compared with other global BA datasets over different years[30]. FireCCIS311 is produced and made available within the ESA's FireCCI project, and distributed through the CEDA catalogue (https://catalogue.ceda.ac.uk/uuid/da8e669a74334c82a56e0b470bc4ef04/), and will soon be operationally processed as part of the Copernicus Climate Change Service.

Differences in inputs and algorithms between the FireCCI51 and FireCCIS311 products constrain the analysis of continuous BA temporal trends over the 21st century, and therefore challenge one of the main objectives of the ESA CCI programme: to generate long-term and consistent time series of Essential Climate Variables (ECVs)[31,32]. In response to this challenge, the harmonisation of these two products is proposed as a strategy to generate a coherent time series that preserves the historical BA coverage provided by FireCCI51 while leveraging the greater detection capability of the FireCCIS311 product. We consider this approach more suitable than the opposite one, which would somehow degrade the Sentinel-3-BA product to resemble the detections from the MODIS sensor. Therefore, our approach aims to maintain the higher accuracy of the FireCCIS311 product while obtaining a longer time series based on FireCCI51 estimates and auxiliary information.

In this context, machine learning models have proven effective for this type of integration, as they can capture nonlinear relationships between satellite and environmental variables and adjust discrepancies between products with different characteristics[33,34]. Our models were trained using the BA estimates from 2019 to 2024, the maximum feasible overlap between FireCCIS311 and FireCCI51 predictor series. FireCCIS311 cannot be extended to years before 2019 because the algorithm depends on Sentinel-3 SYN reflectance derived from OLCI/SLSTR, whose near-daily global coverage only starts in late 2018. Since the official FireCCI51 product ends in 2022, we extended the overlap period by two additional years using a FireCCI51-compatible burned area dataset for 2023-2024[35]. This product was used exclusively as an external input to calibrate the harmonisation models; it is not part of the official FireCCI51 release, since that dataset has been officially generated only until 2022. Due to the post-2022 orbital drift of Terra, the FireCCI51-compatible extended series was generated using a hybrid Terra/Aqua configuration, with Aqua outside the tropics and Terra retained between approximately 20°N and 20°S. Benchmark analyses for 2022 showed that this configuration reproduced the original FireCCI51 annual global BA with a difference of only +0.46% and a mean monthly absolute difference of 1.28%. Consequently, the harmonisation models were calibrated over 2019-2024 and applied retrospectively to 2003-2018. We excluded 2001 and 2002 to avoid biases in the early years of the MODIS sensor, when hotspot detections presented partial gaps due to relying solely on acquisitions from the Terra satellite. From 2003 onwards, the incorporation of Aqua improved hotspot coverage and BA detection[23].

The final product is named *Medium Resolution Burned Area* Grid product version 6.0 (MRBA60) and combines the harmonised historical MRBA60H component (2003-2018) with FireCCIS311 (2019-present). Both components are available as monthly NetCDF files on a 0.25° grid in separate CEDA entries: MRBA60H (https://catalogue.ceda.ac.uk/uuid/db75c5f51ee240ae8743355dcebbb9b9/) and FireCCIS311 (https://catalogue.ceda.ac.uk/uuid/da8e669a74334c82a56e0b470bc4ef04/). The complete MRBA60 series is obtained by temporally concatenating both products, as detailed in the Data Records section.

The new dataset guarantees long-term and consistent analysis of BA trends and facilitates the integration across a wide range of applications, ranging from climate-model evaluation and fire-climate attribution studies to emissions assessments and ecological analyses. Each file is accompanied by detailed metadata documenting variables, units, processing steps, and links to the underlying input products. In the Usage Notes, we discuss key opportunities and limitations of the MRBA60 product, as well as possible directions for future extensions and refinements. We encourage users to build upon this dataset, to compare it with local and regional fire information, and to share feedback and derived products with the fire science community.

Methods

Figure 1 shows the workflow used to generate the harmonised historical MRBA60H component for 2003-2018 and subsequently combine it with the Sentinel-3-derived FireCCIS311 product from 2019 onwards. The resulting continuous time series, spanning from 2003 to the present, is referred to as MRBA60. Our approach included three phases: (1) data preprocessing and generation of a probabilistic BA mask; (2) modelling and calculation of the harmonisation within this mask; and (3) post-processing through bias correction to align the distribution with FireCCIS311. The steps are detailed in the following subsections.

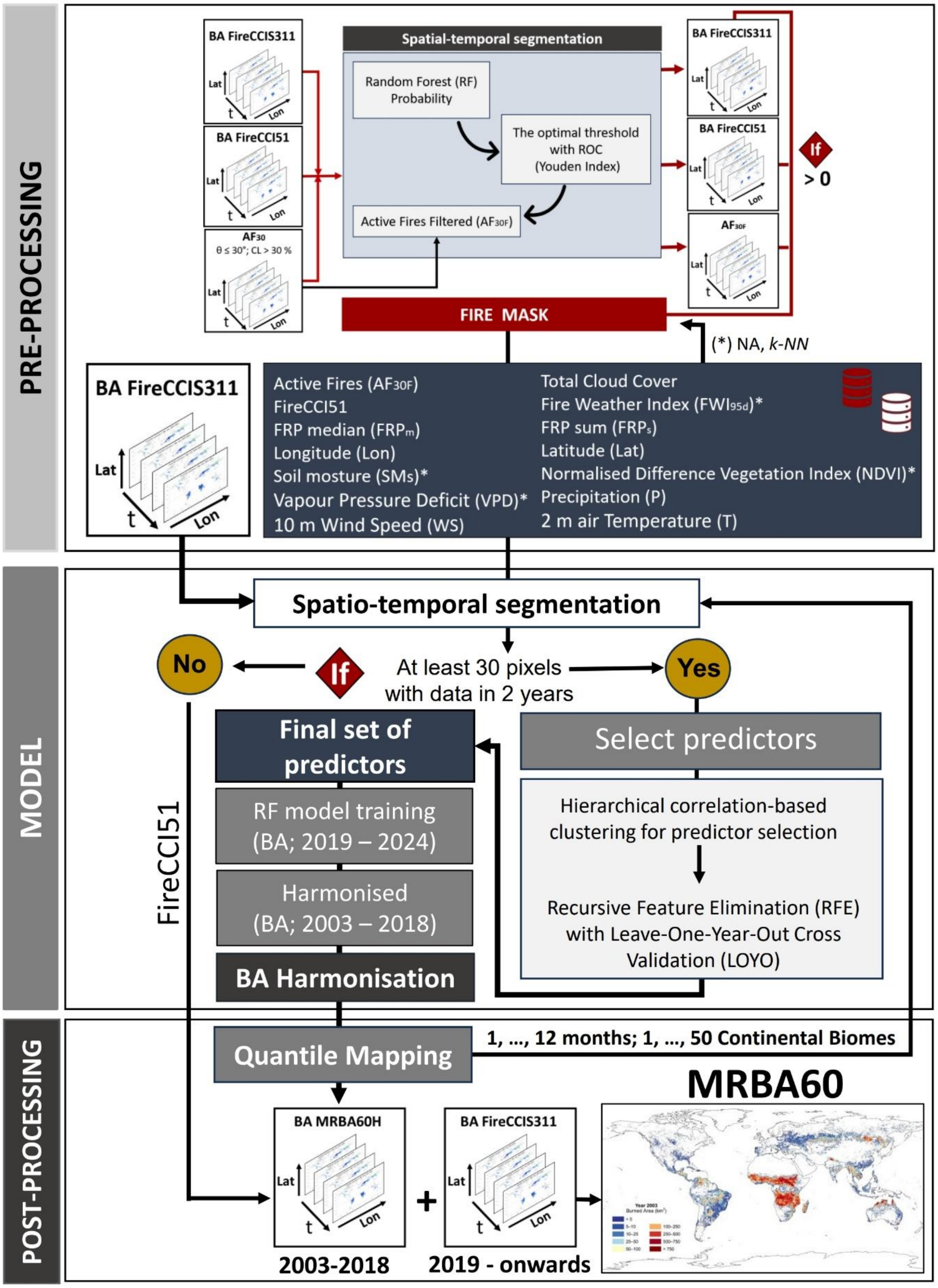

Figure 1. Main structure of the MRBA60 algorithm (2003- onwards).

Pre-processing data and development of the Fire Mask

Datasets

To parametrise the BA predictive model, we used a set of variables that may influence the spatial and temporal patterns of BA during the period 2003-2024. These variables include BA data, AF detections, and Fire Radiative Power (FRP), as well as climatic variables, vegetation indices, and spatial descriptors (Table 1).

Table 1. Summary of the datasets and variables used in the analysis, including their spatial and temporal resolution, units, temporal coverage, and source.

Type	Product	Temporal Res.	Time Period	Spatial Res.	Units	References
Burned area (BA)	FireCCIS3 v.1.1	Monthly	2019 - 2024	0.25°	m^2	Refs.[27,29]
Burned area (BA)	FireCCI v5.1	Monthly	2001 - 2024	0.25°	m^2	Refs.[23,35]
Active fire (AF)	MCD14ML v6.1	Daily	2001 - present	1 km	number of detections	Ref.[36]
Fire Radiative Power sum (FRPs)	MCD14ML v6.1	Daily	2001 - present	1 km	MW	Ref.[36]
FRP median (FRPm)	MCD14ML v6.1	Daily	2001 - present	1 km	MW	Ref.[36]
Mean air temperature (T)	ERA5 (ECMWF)	Monthly	1940 - present	0.25°	K	Refs.[37,38]
Total precipitation (P)	ERA5 (ECMWF)	Monthly	1940 - present	0.25°	m	Refs.[37,38]
Wind speed at 10 m (WS)	ERA5 (ECMWF)	Monthly	1940 - present	0.25°	m/s	Refs.[37,38]
Total Cloud Cover	ERA5 (ECMWF)	Monthly	1940 - present	0.25°	(0 - 1)	Refs.[37,38]
Vapor pressure deficit (VPD)	TerraClimate	Monthly	1958 - present	~0.0417°	hPa	Ref.[39]
Soil moisture (SMs)	GLEAM v4.2b	Monthly	1980 - 2024	0.1°	m^3/m^3	Ref.[40]
Fire Weather Index (FWI)	FWI v4.1	Daily	2003 - 2024	0.25°	numerical	Ref.[41]
Normalised Difference Vegetation Index (NDVI)	MOD13C2 v6.1	Monthly	2000 - present	0.05°	-1 to +1	Ref.[42]
Cell longitude	Longitude	Static	Unique	0.25º	degrees	
Cell latitude	Latitude	Static	Unique	0.25°	degrees	

The final goal of our harmonisation exercise was to generate a BA product that would resemble as much as possible the FireCCIS311 BA estimations to model backwards this product, covering the period when the FireCCI51 dataset was the only one available (2003-2018). To do so, the common period of observations between these two products was used (2019-24).

FireCCI51 was derived from MODIS Terra surface reflectance and MODIS Terra/Aqua AF observations and is available from 2001 to 2024 (but the first two years include higher uncertainty, as only Terra provided AF observations). FireCCIS311 is based on Sentinel-3 SLSTR (as ESA released SYN data at the end of 2018) surface reflectance and VIIRS AF data, and covers 2019 to the present. We based the harmonisation approach on the grid format of both products, which includes the monthly sum of BA at 0.25º × 0.25º. FireCCIS311 was used as the reference for 2019-2024 and provided the BA response variable, while FireCCI51 was used as the predictor variable, along with other auxiliary features (AF, climatic, and vegetation variables).

AF and FRP data are derived from the MODIS MCD14ML product (Collection 6.1), which detects thermal anomalies in the mid-infrared and thermal bands[36]. Following ref.[43], only terrestrial fires, defined as type = 0, were selected. Detections with absolute scan angles >30° (0.5 radians) or confidence values <30% were excluded. The resulting pre-screened AF layer is hereafter referred to as AF30. Valid detections were aggregated monthly onto the global 0.25° grid, computing, per cell, the number of AF30 detections, as well as the sum (FRPs) and median (FRPm) of their corresponding radiative power values in megawatts (MW).

The climatic variables included mean temperature (T), total precipitation (P), wind speed (WS), and total cloud cover, obtained from the European Centre for Medium-Range Weather Forecasts' (ECMWF) Reanalysis v5 (ERA5) data[37,38], available from 1940 onwards at 0.25º spatial resolution. Soil moisture (SMs) was derived from the Global Land Evaporation Amsterdam Model (GLEAM v4.2b)[40], expressed in m^3/m^3, and Vapor Pressure Deficit (VPD) was obtained from TerraClimate[39], based on data from WorldClim[44], Climate Research Unit (CRU Ts4.0)[45], and the Japanese 55-year Reanalysis (JRA-55)[46], with ~4 km (1/24°) resolution and temporal coverage since 1958. The Fire Weather Index (FWI)[47] derived from ERA5 (v.4.1)[41] was used to estimate the number of days with extreme fire conditions (FWI95d), defined as those with FWI above the local monthly 95th percentile[48,49], following the procedure of ref.[50]. The Normalized Difference Vegetation Index (NDVI) was obtained from the MODIS MOD13C2 v6.1 product (0.05°)[42]. All input variables for our model were resampled to a standard 0.25° grid, using conservative interpolation (e.g., Precipitation) or bilinear resampling (e.g., Temperature). Missing values in VPD, SMs, FWI95d, and NDVI, generally in coastal areas, were estimated using spatial interpolation with k-nearest neighbours (*k-NN, k* = 8), ensuring continuous coverage and avoiding inconsistencies (see Supplementary Figure 1). The interpolation was applied only to fire-affected cells containing missing values in the corresponding variable. To avoid selecting ocean neighbours, a binary land-sea mask at 0.25° spatial resolution from the ATLAS/reference-grids repository of the Santander Meteorology[51] Group was used. The *k-NN* searches were restricted exclusively to cells classified as land and containing valid values within the same monthly layer, considering a maximum search distance of eight grid cells. Cells without valid neighbours within this radius remained uninterpolated.

Finally, to capture geographic gradients of fire activity not explained by environmental variables, the latitude and longitude of each cell were incorporated as spatial predictors. That allows the model to represent the spatial heterogeneity of BA better and improve its generalisation capacity across regions and periods[52]. This condition is especially relevant in large continental masses such as Africa, where the climatic influence on fire activity exhibits strong regional and hemispheric variation, also modulated by oceanic and atmospheric circulation[53].

Development of the Fire Mask

Given that FireCCI51 exhibits detection limitations relative to FireCCIS311 during the overlapping period 2019-2024 (with 29% lower global BA), AF30 (defined above as the pre-screened AF layer retaining terrestrial detections with scan angles ≤30° and confidence values ≥30%) was incorporated as an auxiliary source to recover part of the signal potentially missing in FireCCI51. However, integrating AF detections requires a dedicated assessment, since AF30 may include thermal signals that do not necessarily translate into burned-area scars, and may even capture events that FireCCIS311 (the reference product) does not record; this is particularly relevant because the aim is for the harmonised product to resemble FireCCIS311, rather than to introduce additional discrepancies. Therefore, the pre-screened AF30 detections, FireCCI51, and FireCCIS311 were classified into possible combinations (exclusive detections, pairwise matches, and triple matches), which allowed the derivation of three operational indicators: (i) simultaneous matches between all three products (robust detection), (ii) matches between AF30 and FireCCIS311 without FireCCI51 (candidate burned cells), and (iii) exclusive AF30 detections, considered as possible false detections, since they were not detected by either of the other two products during the overlapping period 2019-2024. During the common period, matches among the three products accounted for 47-52% of total detections; the AF30 + FireCCIS311 pair contributed an additional 20-23%; and exclusive AF30 detections ranged between 16-18%.

To remove potentially spurious AF30 detections, a two-stage filtering was applied before AF30 was allowed to contribute to the final Fire Mask. First, a probability that AF30 detections correspond to BA was generated through a Random Forest (RF)[54], following ref.[33], with *ntree* = 250 and *mtry* = 1, using AF30 and FireCCI51 as predictors. Training was performed on a per-region basis, using modified continental biomes[55] (see Supplementary Table 1) for 2019-2024, defining presence as FireCCIS311 recording BA > 0 and absence otherwise. For each region and target month, an independent model (hereafter, a region-month model) was fitted using data from a moving three-month window to capture seasonality (e.g., December-January-February for January; January-February-March for February; etc.). In addition, region-month models with fewer than 30 cells with preliminary *Mask* = 1 (defined as fire evidence: AF30 or FireCCI51 or FireCCIS311 > 0, in at least 2 years) were excluded to avoid unstable estimates due to limited sample size. This preliminary mask was used only to define the RF training domain and is distinct from the final Fire Mask used to constrain harmonisation. In total, 579 independent models were fitted. When probabilities could not be estimated, the FireCCI51 value was retained (Supplementary Figure 2).

In the second stage, filtering was based on Receiver Operating Characteristic curves (ROC)[56,57], generated from region-month combinations for 2019-2024. Presence of BA was defined when FireCCI51 or FireCCIS311 detected BA > 0; absence of BA was defined when the detection was exclusive to AF30. The optimal threshold was determined using the Youden index[58], selecting the point that simultaneously maximizes sensitivity (detection of effectively burned cells) and specificity (exclusion of potential false AF30 detections). We evaluated the discriminatory ability of the threshold using the Area Under the Curve (AUC)[57]. Filtering was applied only when the AUC was significant, using False Discovery Rate (FDR) correction (adjusted $p < 0.05$)[59,60]. In those cases, the optimal probability threshold estimated for 2019-2024, derived from the ROC curves using the Youden index, was extrapolated to the entire AF30 series (2003-2018). AF30 value was set to zero when the estimated probability fell below the optimal threshold, and no independent BA evidence was found in FireCCI51 or FireCCIS311. Thus, AF30F was generated. As a result, exclusive AF30 detections decreased from 35-43% to 14-19% (AF30F) in 2003-2018, and AF30-FireCCI51 coincidence increased from 54-62% to 75-79% (AF30F-FireCCI51). Finally, the final Fire Mask was generated from FireCCI51, FireCCIS311, and AF30F. A cell was assigned Fire Mask = 1 when FireCCI51 or FireCCIS311 detected BA, or when AF30F retained a filtered AF detection after the RF-ROC procedure; otherwise, Fire Mask = 0. Harmonisation was restricted to cells with *Fire Mask* = 1, preventing artificial BA generation in areas without fire evidence. The Fire Mask was therefore used only as an eligibility domain for harmonisation; it did not assign BA values by itself.

Harmonisation model

To build the predictive models for each region-month combination (i.e., each modified continental biome and target month, using a centred three-month moving window), we performed a model-specific predictor selection before model fitting. Specifically, starting from an initial set of N candidate predictors, we identified for each region-month model a parsimonious subset ($M < N$) to reduce multicollinearity and maximise out-of-sample predictive performance. We applied a two-step procedure following ref[33,61]. First, for each region-month combination, we computed the Spearman correlation (ρ) matrix among all candidate predictors (2019-2024) and transformed it into a distance matrix ($d_{xy} = 1 - |\rho_{xy}|$). Groups of highly correlated predictors were identified using complete-linkage hierarchical clustering[61], cutting the dendrogram at height h = 0.3 and imposing a similarity ≥ 0.7[33]. From each cluster, we retained the variable showing the highest absolute correlation with FireCCIS311. Second, this reduced set was further refined using RF and Recursive Feature Elimination (RFE) with Leave-One-Year-Out (LOYO) validation. We evaluated the predictive accuracy of increasing predictor subsets (from 1 to p), using *ntree* = 250 and *mtry* = p/3 (default for RF regression)[62] within the caret R package (v7.0-1)[63], which uses Root Mean Squared Error (RMSE) as the optimisation metric for regression. Therefore, the final predictor set for each region-month model was selected as the subset yielding the lowest RMSE. Region-month combinations with insufficient training data (i.e., fewer than 30 cells with *Fire Mask* = 1 in at least two years) were excluded from model fitting, and in those cases, values were taken directly from FireCCI51.

Across the ensemble of region-month models, predictors were selected with different frequencies, reflecting regional and seasonal differences in the relationships between BA and its drivers (Supplementary Figure 3). FireCCI51 was the predictor most frequently retained (99% of models), followed by longitude, latitude, and NDVI (>70%). In contrast, the remaining predictors appeared in ~55-70% of models, except for FRPm and FRPs, which were included in 15-25% of models, respectively (Supplementary Figure 3). Predictor importance within each fitted model was assessed using SHAP values (SHapley Additive exPlanations)[64], and summarised in Supplementary Figure 4. Considering jointly ranks 1 and 2, FireCCI51 was among the two most important predictors in 459 models (254 times ranked first), followed by count AF30F with 325 (188 times ranked first) and FRPs with 140 (74 times ranked first). That indicates that although FRP variables entered a relatively small fraction of models (Supplementary Figure 3), they contributed substantially to model fit.

Finally, the trained models were applied retrospectively to the FireCCI51 time series (2003-2018) to predict what FireCCIS311 would have mapped during this period. This dataset was named MRBA60H. For this historical reconstruction, the model corresponding to each region-month combination was applied. However, a well-known limitation of machine-learning models such as RF is their inability to extrapolate beyond the range observed during training[54]. In particular, RF cannot generate BA values higher than the maximum observed in the calibration data because predictions are based on averages of previously observed values[54]. Consequently, when applying the model to 2003-2018, some extreme BA episodes might have been underestimated if they were not represented in the training period (2019-2024). To avoid truncation of extremes, we defined for each region-month combination a maximum threshold (BAmax) as the maximum FireCCI51 value observed in 2019-2024, computed using a centred three-month moving window. During the generation of the MRBA60H product, when the FireCCI51 value (2003-2018) exceeded BAmax, the original FireCCI51 value was retained rather than the model prediction, so that RF's limited extrapolation capability did not artificially decrease extremes outside the training range. This rule affected ~0.13% of monthly cells (4,201 out of 3,327,921 with BA > 0), and therefore, we can consider that the modelling period included broad enough conditions to estimate the historical variability of extremes in most regions consistently.

Post-processing

A final step was applied to generate the MRBA60H in order to compensate for the tendency of the RF models to regress toward the mean[54], which compresses the lower and upper tails of the predicted distribution, reduces the prediction of extremes, and increases the frequency of central values. To mitigate this effect, a bias correction was performed through empirical Quantile Mapping (QM)[65] to improve the resemblance of the harmonised product to that of FireCCIS311. This method reduces systematic discrepancies in the frequency distribution of BA values, while preserving the temporal and spatial coherence of the series. QM has been previously applied to fire-related variables, for example, to correct biases in seasonal Fire Weather Index forecasts[66], and in ref.[7] to reduce systematic biases in vegetation-cover fields that propagate into burned-area responses in the modelled scenarios.

The bias correction was calibrated over the overlap period 2019-2024, using FireCCIS311 as the reference product (and the harmonised product as the series to be corrected), and applying a spatiotemporal stratification consistent with the modelling framework, i.e., by region-month combination (modified continental biome and target month, using a centred three-month moving window). QM was estimated with a quantile resolution of 0.01. The resulting transformation, which maps the quantiles of the harmonised product onto those of FireCCIS311, was applied to the 2003-2018 period through linear interpolation between quantiles[67]. QM correction was restricted to observations with BA > 0 and was not applied to values retained for exceeding BAmax, nor to region-month combinations that did not meet the minimum training criteria (i.e., region-month models with fewer than 30 cells with Mask = 1 in at least two years), for which values were taken directly from FireCCI51. Finally, corrected values were adjusted to ensure physical validity by setting BA values below the area equivalent to a 300 m pixel (the minimum observed BA in the Sentinel-3 SYN BA pixel product) within a 0.25° grid cell to zero, with this threshold computed as a function of latitude. This threshold was derived from the nominal area of a 300 m pixel at the equator (~0.09 km^2), scaled by the cosine of the grid-cell central latitude. The maximum monthly BA was also constrained to the physically available area of each grid cell. This maximum area was likewise estimated as a function of latitude, using the equatorial area of a 0.25° × 0.25° cell (~769 km^2) scaled by the cosine of the grid-cell central latitude, thereby accounting for the progressive decrease in grid-cell area towards higher latitudes[68].

Figure 2 summarises the calibration period (2019-2024), comparing FireCCI51, FireCCIS311, and the harmonised product at the cell-month level. In Figure 2a, the yellow points represent FireCCI51 against FireCCIS311. An underestimation is observed by FireCCI51, as the regression line (solid black) lies below the 1:1 diagonal (dashed black). The metrics indicate a positive but moderate relationship (R^2 = 0.77; Spearman Correlation = 0.78; RMSE = 30 km^2; Y = -0.0147 + 0.8734x). In the inset density plot (X-axis on a logarithmic scale; Y-axis in %), FireCCI51 shows a higher frequency of intermediate values, while FireCCIS311 accumulates more very low values, suggesting that FireCCI51 under-represents small BA events and shifts the distribution toward larger areas, contributing to the observed bias. In Figure 2b, the orange points represent the harmonised product against FireCCIS311. The regression line nearly overlaps the 1:1 diagonal, with low scatter, indicating a substantial reduction in bias and an almost perfect correspondence (R^2 = 0.97; Spearman Correlation = 0.93; RMSE = 7.6 km^2; Y = 0.8710 + 1.0136x). In the density distribution, the curves for the harmonised product and FireCCIS311 coincide closely; the harmonised product shows slightly lower density at very low values and somewhat higher density at medium and high values. Overall, harmonisation in the common period preserves the statistical structure and coherence of the reference product.

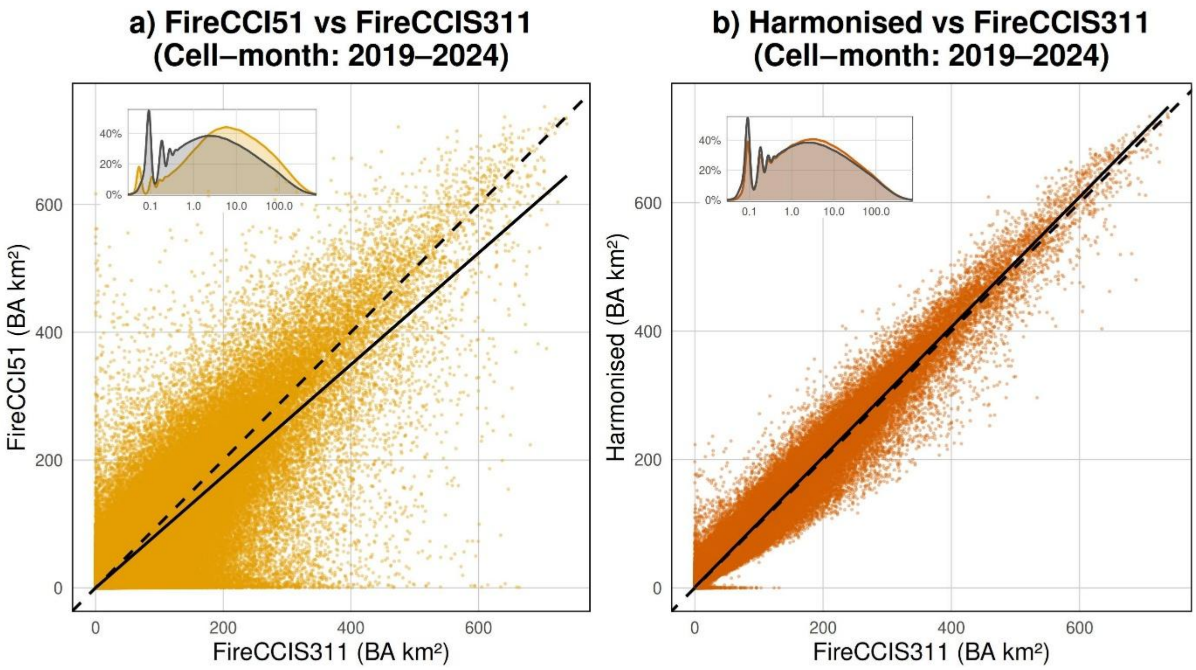

Figure 2. Performance of the harmonisation during the training period (2019-2024). Panel a) compares FireCCI51 and FireCCIS311 at the cell-month level. Panel b) shows the same comparison, but for the harmonised product and FireCCIS311. In both panels, the black solid line represents the linear regression, and the black dashed line the 1:1 diagonal. Insets display the density distribution of burned area on a logarithmic x-axis, with the y-axis showing density in percent, and colours: FireCCI51 (yellow), Harmonised (orange), and FireCCIS311 (grey).

Supplementary Figures 6-10 show seasonal and annual relative-frequency analyses to evaluate what QM contributes to the harmonisation during 2003-2018. The analysis was conducted at the grid-cell level, accumulating BA within each season or year, without spatially aggregating cells within each region. Since both Harmonisation (RF only) and MRBA60H (RF + QM) incorporate the same FireCCI51-based extreme-restoration procedure, applied to approximately the upper 0.13% of extreme values (see the Harmonisation model section), the comparison between both products allows the effect of QM on the overall shape of the relative frequencies to be evaluated while keeping the treatment of extremes constant. Regional analyses follow the fire-region framework defined in ref.[69] (see Supplementary Figure 5). At the global scale, QM shifted the distribution towards smaller burned-area values. The frequency of grid cells below 1 km² increased from 3.8% to 5.7% in the annual analysis and from 4.5-7.7% to 8.0-9.3% across seasons. This increase was accompanied by a systematic reduction in the 1-10 km² class, from 32.1% to 29.0% annually and from 39.8-47.5% to 35.2-43.1% seasonally, indicating that QM mainly redistributes moderate small-fire values towards the lowest burned-area class. By contrast, the 10-100 km² class remained comparatively stable, changing from 39.8% to 39.6% annually, while the >100 km² class within the analysed range increased only modestly, from 24.3% to 25.7% annually. Regionally, this lower-tail redistribution was most pronounced in Equatorial Asia (EQAS), where the <1 km² class increased by 14.9 percentage points in December-January-February (DJF) and 21.5 percentage points in March-April-May (MAM), with corresponding reductions of 13.7 and 18.2 percentage points in the 1-10 km² class. Temperate North America (TENA) and Boreal North America (BONA) also showed marked reductions in the 1-10 km² class, reaching 8.5 percentage points annually in TENA and 5-8 percentage points across seasons in BONA. In contrast, the annual distributions in Northern Hemisphere Africa (NHAF) and Southern Hemisphere Africa (SHAF) changed much less, with shifts of less than 1 percentage point in the <1 km² and >100 km² classes, consistent with a more stable upper tail in regions with extensive and recurrent fire activity. The comparison with Global Fire Emissions Database (GFED5.1)[43,70,71] and MCD64A1 (Collection 6.1)[72,73] provides external context, suggesting that MRBA60H (RF + QM) preserves high frequencies of large burned-area values in high-fire-activity regions while remaining broadly consistent with the range of behaviour observed in other global BA products.

Uncertainty

In addition to the BA estimates, we assessed the uncertainty of the harmonised product at the grid cell level using an empirical approach developed for non-parametric methods[74], employing the RMSE as a standard metric to evaluate discrepancies between predictions and observations. The analysis was conducted by continental biome, using 2019-2024, the common period between FireCCIS311 and the harmonised product, as the calibration window. For each biome, prediction-observation pairs were stratified into 10 bins defined by prediction quantiles, and the absolute RMSE was estimated within each bin. Based on these estimates, a linear model of the error as a function of predicted magnitude was fitted and applied to the entire 2003-2024 series to generate maps of absolute uncertainty. Values were constrained to physically plausible BA ranges. Additionally, we computed the RMSE of the harmonised product against FireCCIS311, and separately FireCCI51 against FireCCIS311. With this, in cells that could not be harmonised and retained the FireCCI51 value (due to a lack of training data in a given biome/month or to exceeding the threshold observed during training), it was possible to assign an uncertainty consistent with FireCCI51's performance. That process ensured the spatial continuity of RMSE maps during the 2003-2018 period. From 2019 onwards, when MRBA60 directly incorporates FireCCIS311 values, the modelled RMSE is replaced by the Standard Error (SE, m²) layer of the FireCCIS311 product itself[24]. The uncertainty characterisation in FireCCIS311 is based on indices derived from SLSTR reflectance at 300 m resolution, with burn probabilities subsequently aggregated to 0.25° grids using a Poisson binomial distribution approach[75].

Spatial coherence of these estimates is illustrated in Supplementary Figure 11, which shows the BA estimates and RMSE for August 2003, where the highest RMSE values are observed in regions with higher BA. These estimates should be interpreted as an empirical, first-order approximation of the uncertainty of the BA product, and not as a complete theoretical characterisation of uncertainties in BA products, as discussed by ref.[76].

Data Records

The MRBA60H version 6.0 dataset is archived at the Centre for Environmental Data Analysis (CEDA) as a versioned collection of NetCDF files (https://catalogue.ceda.ac.uk/uuid/db75c5f51ee240ae8743355dcebbb9b9/)[77]. The dataset provides global monthly BA estimates for the period 2003-2018 on a regular 0.25° × 0.25°

geographic grid in WGS84 coordinates. Each file corresponds to a full calendar month and is identified by the first day of the month in YYYYMMDD format. The naming convention is:

<Indicative_Date>-ESACCI-L4_FIRE-BA-MR_HAR-fv<xx.x>.nc

where <Indicative_Date> identifies the date, MR_HAR denotes the harmonised medium-resolution BA dataset, and fv<xx.x> indicates the dataset version.

The MRBA60H files follow CF-1.7 metadata conventions and include the dimensions *lon* (longitude), *lat* (latitude), time, and bounds. The global grid contains 1440 longitude cells and 720 latitude cells. Each file contains a single monthly time step. Longitude and latitude coordinates correspond to the centre of each 0.25° grid cell and are provided in decimal degrees together with their spatial bounds. The time variable is expressed as days since 1970-01-01 00:00:00 following CF-1.7 temporal encoding conventions using the standard calendar, with temporal bounds corresponding to the month.

The variables provided in MRBA60H are *burned_area* and uncertainty, both stored with dimensions *time* × *lat* × *lon. burned_area* represents the sum of monthly BA in each grid cell, expressed in m^2, while uncertainty provides the associated uncertainty, also in m^2. Both variables include attributes such as units, descriptive names, valid range, and missing-value conventions. The metadata of the NetCDF files include global attributes describing the DOI, processing level, source datasets, temporal and spatial coverage, processing history, contact information, and licence. The dataset follows a versioned release scheme using the fv<xx.x> convention.

For analyses requiring the continuous 2003-present record, the MRBA60 series is obtained by temporally concatenating the monthly MRBA60H files for 2003-2018 with the monthly FireCCIS311 0.25° grid files from 2019 onwards, distributed through a separate CEDA entry (https://catalogue.ceda.ac.uk/uuid/da8e669a74334c82a56e0b470bc4ef04/). Users should order the files by their indicative date and concatenate them along the time dimension, retaining *burned_area* as the common burned-area variable. No spatial regridding or unit conversion is required. Supplementary Code 1 provides an example CDO-based Bash script for extracting the common *burned_area* variable, harmonising latitude orientation when required, and concatenating the monthly files along the time dimension. To facilitate product use, ensure operational continuity, and streamline the transfer of the Sentinel-3-derived processing chain to the Copernicus Climate Change Service, from the next update, scheduled for late 2026, the grid files corresponding to the post-2018 period will be distributed under the MRBA60 naming convention. However, these files will remain available as a separate component from the historical MRBA60H record, and users will need to temporally concatenate both components to obtain the complete MRBA60 series. Annual updates of the MRBA60 series are planned as data corresponding to new years become available, preserving the same file structure, spatial grid, variable naming conventions, and metadata standards to ensure backward compatibility across releases.

An auxiliary monthly harmonisation status mask was generated for 2003-2018 to document the origin of each grid-cell estimate using three classes: 0 = no burned-area estimate, including unburned or non-burnable cells; 1 = value harmonised using RF and QM correction; and 2 = value retained from FireCCI51. The mask has been deposited as a complementary dataset in the Zenodo data repository (see Data availability section)[78]. This provenance mask is limited to the 2003-2018 period, corresponding to the reconstructed MRBA60H component. From 2019 onwards, MRBA60 directly adopts the FireCCIS311 burned-area estimates without applying any additional harmonisation or reconstruction step. Consequently, provenance after 2018 is unambiguous, as all valid burned-area estimates originate from FireCCIS311.

Technical Validation

The global validation of FireCCI products relied on a Landsat-based burned-area reference dataset organised on a Thiessen Scene Area (TSA) sampling framework[28,29]. In this study, we used an updated version of this reference dataset covering 2017-2024. Figure 3a shows the spatial distribution of the TSA for 2017-2024, as well as the regions with validation and intercomparison data used in this study. Each TSA corresponds to a spatial sampling unit of approximately 100 × 100 km, on which long temporal units are constructed from consecutive Landsat 8 and 9 image pairs (with ≤16 days between acquisitions and low cloud cover). The reference BA polygons included three categories: (1) BA including all polygons detected as burned; (2) the no-data category polygons that could not be interpreted or were not observed by the sensor due to clouds and/or cloud shadows, topographic shadows, smoke, or sensor errors; and (3) the unburned category that includes all polygons observed as unburned within the image coverage limits. In addition, each polygon includes the pre- and post-fire image dates (*preDate* and *postDate*), using the latter to assign the month of BA occurrence[29,30].

To enable comparability with the harmonised product, the reference BA polygons were overlaid onto the 0.25° grid. For each grid cell, the reference BA was computed by summing the area of all category-1 polygons within each 0.25° cell. Cell-months fully covered by category-2 (no-data) polygons were excluded from the analysis. In contrast, when category-2 and category-3 (unburned) polygons co-occurred within the same cell, the cell was retained and assigned BA = 0. Thus, for each 0.25° cell and month (based on *postDate*), an aggregated BA reference value was obtained, consistent with the spatial and temporal resolution of the harmonised product. This overlay and rasterisation process of TSA polygons to the 0.25° grid is illustrated in Figure 3b. The TSA at 0.25º has been deposited as a complementary dataset in the Zenodo data repository (see Data availability section)[79].

In addition to the TSA, comparisons were made with FireCCI regional high-resolution products, named FireCCISFDL10[80,81] (generated from Landsat data at 30 m). This dataset covers three regions: Amazonia (24°S-12°S; 47°W-62°W), Eastern Sahel (4°N-16°N; 27°E-43.5°E) for the period 1990–2019, and Siberia (63°E-180°E; 58°N-74°N) for the period 1990–2022. They were generated using a multitemporal classification of spectral indices, followed by contextual patch refinement[80,81].

As a complementary analysis, the ONFIRE dataset[82,83] was used for intercomparison with MRBA60 results. ONFIRE harmonises official BA records based on governmental inventories from Australia, Canada, Chile, Mediterranean Europe, and the United States, resampled to a regular 1° × 1° grid and a monthly temporal resolution. In Australia, the dataset is based on operational fire management records and the Northern Australian Fire Information (NAFI) system. In Canada, the National Fire Database (NFDB, point records of fires >2 km^2) and the National Burned Area Composite (NBAC, fire perimeters derived from 30 m Landsat images), compiled by federal and provincial forest agencies, are used. In Chile, data come from the National Forest Corporation (CONAF), which provides monthly statistics by administrative region and cover type based on BA polygons in natural vegetation and forest plantations. In the United States, the Fire Program Analysis Fire-Occurrence Database (FPA-FOD, recording fires from ~0.0004 km^2 and excluding prescribed or controlled burns) and the Monitoring Trends in Burn Severity (MTBS) program, which maps perimeters of large fires detected using Landsat, with minimum size thresholds of 2.02 km^2 in the east and 4.05 km^2 in the west, are combined. For Europe, ONFIRE uses monthly data voluntarily submitted by Member States to the European Forest Fire Information System (EFFIS), aggregated at the NUTS3 level and focused on forest areas and other non-agricultural natural land. In this study, we focused on the Iberian Peninsula, southern France, and part of Italy, where ONFIRE provides the most complete and consistent coverage over time.

Additionally, the MapBiomas Fire product (Collection 4.1), which maps annual BA in Brazil at 30 m using annual Landsat mosaics and deep learning algorithms for the 1985-2024 period[84], was used. For intercomparison with MRBA60, the 30 m burned pixels were resampled to a 0.25° grid. In this process, each native pixel was transferred to the new grid system and assigned a weight proportional to the cosine of latitude, which approximates the true surface area of the land pixel under the geographic projection (WGS84). Subsequently, the weighted values of all pixels assigned to each 0.25° cell were summed to obtain the annual total BA within each spatial unit.

Finally, the FireCCISFD11 product, derived from 2016 Sentinel-2A MSI data, which generated a wall-to-wall BA classification at 20 m for sub-Saharan Africa and was also available in 0.25° grid format[85], was used as an additional reference for regional intercomparison.

Additionally, a global intercomparison of the MRBA60 series with other widely used BA products, including the BA component of the Global Fire Emissions Database (GFED5.1)[43,70,71] and the NASA MCD64A1 (Collection 6.1)[72,73], was performed. The former combines multiple remote sensing data sources to model a monthly BA dataset at 0.25° spatial resolution covering the period 1997-2022[43]. For GFED5, the data corresponding to 2023 and 2024 were beta releases (*GFED5.1ext_Beta*)[71] that have not yet been formally validated and are made available as preliminary products through the portal (https://www.globalfiredata.org/data.html). The MCD64A1 is derived from MODIS and combines spectral change detection and AF information to map burned surfaces at 500 m spatial resolution in a continuous time series since 2000[72,73].

In the following validation and intercomparison sections, MRBA60H and FireCCIS311 are considered jointly as MRBA60, without distinguishing between the pre- and post-2019 periods, as the product is evaluated and analysed as an integrated time series.

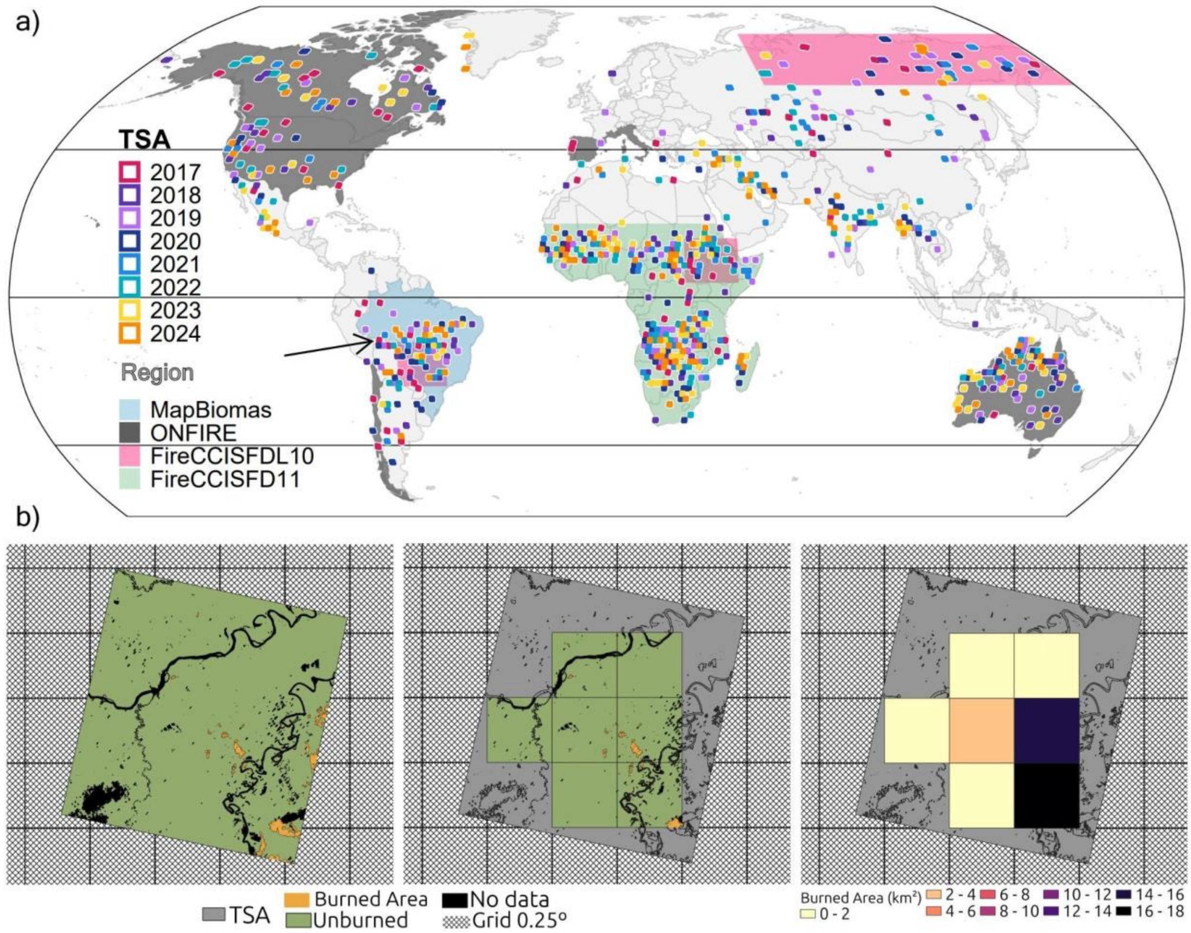

Figure 3. Regions with validation and intercomparison data used in this study. (a) Spatial distribution of the reference Thiessen Scene Areas (TSA) for 2017-2024 (106 TSA per year) and locations of the intercomparison areas covered by FireCCISFDL10, ONFIRE, MapBiomas Fire, and FireCCISFD11. (b) Schematic of the rasterisation of TSA polygons onto a uniform 0.25° grid (i.e., the MRBA60 resolution) for the monthly calculation of reference burned area. The arrow in panel (a) indicates the TSA unit used in the rasterisation example shown in panel (b).

Validation with 2017-2024 Landsat scenes

Table 2 summarises the spatial validation of MRBA60 against the annual BA derived from TSA for 2017-2024, and compares it with FireCCI51, MCD64A1, and GFED5. Overall, MRBA60 and GFED5 show the best agreement with the TSAs, with correlations close to 0.9, R^2 values generally greater than 0.8, a moderate RMSE, and regression slopes close to unity, indicating a close-to-identity fit. As a representative example, 2018 is a particularly favourable year for MRBA60, with a correlation of 0.90 ($p < 0.05$), an RMSE of 53 km^2, and a slope of 0.87. By contrast, 2022 shows a less favourable performance in terms of error: the RMSE for MRBA60 is higher than that for GFED5 and FireCCI51 (51 km^2 compared with 47 and 50 km^2, respectively), and the slope decreases to 0.7, although MRBA60 maintains a high correlation of 0.88 ($p < 0.05$). MCD64A1 generally shows the lowest correlation and the highest RMSE, indicating a poorer fit relative to the TSA, and a strong bias towards underestimating BA. FireCCI51 shows intermediate performance in the available years. The BIAS (%) quantifies the relative bias of each product's annual total with respect to the total observed by the TSA. Therefore, negative values indicate an underestimation of BA relative to the TSA. The scatter plots and regression lines for the eight years are shown in Supplementary Figure 12.

Table 2. Spatial validation metrics of the global burned area products against the annual burned area reference from Thiessen Scene Areas, using *n* as the number of valid 0.25° grid cells available for validation in each year; 106 Thiessen Scene Areas were available each year. This TSA-based validation evaluates the integrated MRBA60 time series, combining the harmonised historical component for 2017-2018 (MRBA60H) and the direct FireCCIS311 component for 2019-2024.

Years	Dataset	Spearman Correlation	R^2	RMSE (km^2)	MAE (km^2)	BIAS (%)	Intercept (km^2)	Slope
2017 (n=946)	MRBA60	0.90	0.79	76	34	-19	5.87	0.75
	FireCCI51	0.89	0.75	82	35	-22	0.98	0.77
	MCD64A1	0.86	0.65	101	46	-36	4.34	0.59
	GFED5	0.88	0.81	70	32	-7	8.26	0.84
2018 (n=870)	MRBA60	0.90	0.91	53	22	-13	-0.13	0.87
	FireCCI51	0.89	0.88	62	26	-23	-4.41	0.82
	MCD64A1	0.88	0.80	82	34	-33	-5.78	0.73
	GFED5	0.90	0.89	60	27	-17	3.37	0.79
2019 (n=896)	MRBA60	0.90	0.89	57	25	-26	-1.74	0.76
	FireCCI51	0.86	0.84	62	28	-27	-5.01	0.79
	MCD64A1	0.85	0.82	71	31	-36	-4.41	0.70
	GFED5	0.88	0.85	56	25	-8	5.38	0.85
2020 (n=911)	MRBA60	0.90	0.77	75	34	-38	-1.18	0.63
	FireCCI51	0.86	0.71	81	36	-42	-3.46	0.63
	MCD64A1	0.83	0.64	92	43	-49	-3.27	0.55

	GFED5	0.87	0.80	62	29	-15	2.21	0.82
2021 (n=897)	MRBA60	0.90	0.88	72	29	-31	1.45	0.67
	FireCCI51	0.86	0.84	78	33	-35	-1.97	0.67
	MCD64A1	0.85	0.75	95	40	-46	-3.05	0.58
	GFED5	0.88	0.87	62	26	-18	4.63	0.77
2022 (n=812)	MRBA60	0.88	0.92	51	20	-25	1.98	0.70
	FireCCI51	0.81	0.91	50	20	-26	-1.13	0.76
	MCD64A1	0.77	0.84	64	25	-33	-0.40	0.68
	GFED5	0.84	0.91	47	20	-10	6.40	0.79
2023 (n=840)	MRBA60	0.93	0.77	80	37	-25	4.73	0.70
	FireCCI51	0.87	0.75	84	40	-31	-0.69	0.70
	MCD64A1	0.85	0.58	109	50	-40	3.24	0.56
	GFED5	0.93	0.82	68	32	-4	7.44	0.88
2024 (n=825)	MRBA60	0.92	0.82	66	29	-22	5.84	0.71
	FireCCI51	0.86	0.77	75	35	-32	1.63	0.66
	MCD64A1	0.87	0.71	85	38	-39	2.04	0.59
	GFED5	0.93	0.77	68	32	-7	14.18	0.75

Intercomparison with regional products

Figure 4 shows an intercomparison of global BA products against annual reference estimates in six regions: Amazonia, the Sahel, and Siberia (FireCCISFDL10), Brazil (MapBiomas), Australia, and Canada (ONFIRE). As with the global products, the reference datasets used (FireCCISFDL10, MapBiomas, and ONFIRE) incorporate methodological and observational uncertainties and, in some cases, are not entirely independent of the evaluated products (for example, Australia-ONFIRE integrates state inventories and NAFI fire scar maps derived from MODIS, the same sensor used by MRBA60, FireCCI51, and MCD64A1)[82]. Consequently, the reported metrics (see also Supplementary Table 2) quantify agreement and systematic differences relative to the selected reference, and apparent “overestimations” or “underestimations” should be interpreted as deviations that may reflect errors in any of the datasets or differences in definitions and in detection sensitivity.

In Amazonia (Figure 4a), MRBA60 captures the interannual variability of FireCCISFDL10, with a high correlation (0.94; $p < 0.05$), an RMSE of 23,295 km², a slope very close to identity (1.08), and a bias relative to FireCCISFDL10 of -20%. GFED5 shows the best performance in this region, with a correlation of 0.97 ($p < 0.05$), an RMSE of 9,705 km², a slope of 0.84, and a BIAS of 5%. The suitability of FireCCISFDL10 as a reference product in Amazonia is supported by the independent regional validation by ref.[30], which reports commission and omission errors below 10%, a Dice Coefficient (DC) greater than 90%, and a relative bias of approximately -2.5%. In the Sahel (Figure 4b), where performance of FireCCISFDL10 was lower than in Amazonia[30], MRBA60 and FireCCI51 show the same moderate-to-high correlation (0.83; $p < 0.05$), with RMSE values of 36,593 km² and 36,854 km², slopes close to identity but slightly lower for MRBA60 than for FireCCI51 (0.89 and 0.95, respectively), and positive BIAS value (5% and 3%, respectively). MCD64A1 shows a higher correlation (0.86; $p < 0.05$), but with an RMSE of 68,631 km², a slope of 0.81, and a negative bias of -15%. GFED5 shows the lowest correlation (0.72; $p < 0.05$), the highest RMSE (129,162 km²), a slope of 0.95, and a positive bias of 31%. Independent validations of FireCCISFDL10 estimated in ref.[29] for this region showed a relative bias of -18.6% and an omission error of 34.8%, suggesting that part of the positive bias observed relative to FireCCISFDL10 could be influenced by an underestimation in the reference product in the Sahel. In Siberia (Figure 4c), MRBA60 shows high interannual consistency with FireCCISFDL10, with a correlation of 0.94 ($p < 0.05$), an RMSE of 12,064 km², a slope of 0.85, and a BIAS of -23%. GFED5 shows the greatest temporal consistency (0.98; $p < 0.05$), with an RMSE of 13,958 km², a slope of 1.25, and a BIAS of 26%. FireCCI51 maintains a similar behaviour to MRBA60 (0.94; $p < 0.05$), with an RMSE of 15,546 km², a slope of 0.85, and a BIAS of -34%. Additionally, MCD64A1 shows a high correlation (0.94; $p < 0.05$), the highest RMSE (21,351 km²), the lowest slope (0.71), and a BIAS of -42%. The independent regional validation of ref.[30] reports a relative bias of -76.4% for FireCCISFDL10 in Siberia, with commission and omission errors on the order of 54.3% and 89.2%, respectively. Nevertheless, these results should be interpreted with caution, as this validation was conducted within a spatially constrained domain (60°N-74°N; 65°E-87°E), which is not strictly equivalent to the regional extent considered in this study[80].

In Brazil (MapBiomas, Figure 4d), MRBA60 captures interannual variability, with a high correlation (0.92; $p < 0.05$), an RMSE of 86,116 km², a slope of 1.51, and a BIAS of 39%. FireCCI51 and MCD64A1 show similar temporal consistency with the same correlation (0.91; $p < 0.05$), with lower errors (RMSE of 40,031 km² and 30,937 km²) and slopes of 1.28 and 1.15; their differences remain close to zero, with BIAS of -2% and 1%, respectively. GFED5 shows the lowest agreement with MapBiomas, with a lower correlation (0.78; $p < 0.05$), the highest error (RMSE of 161,424 km²), a slope of 1.19, and a BIAS of 94%. Nevertheless, this difference should be interpreted as a relative discrepancy, since MapBiomas may under detect BA (i.e., large differences were observed against FireCCISFDL10).

In Australia (Figure 4e), MRBA60 shows high temporal consistency against ONFIRE, with a high correlation (0.97; $p < 0.05$), an RMSE of 38,414 km², a slope very close to identity (1.03), and a relative bias of 7%. FireCCI51 is comparable to MCD64A1 in terms of correlation (0.96), but it exhibits a higher RMSE (53,584 versus 40,459 km²) and a lower slope (0.89 versus 1.04), with negative BIAS in both cases (-8% and -6%). In Canada (Figure 4f), against NBAC-ONFIRE, MRBA60 shows high temporal consistency (correlation of 0.87; $p < 0.05$) of all BA products, with an RMSE of 8,760 km², a slope of 1.02, and a BIAS of 51%. FireCCI51 shows similar consistency (correlation of 0.89; $p < 0.05$), with an RMSE of 4,791 km², a slope of 0.86, and a BIAS of 17%. In contrast, GFED5 shows clearly larger discrepancies in this region (RMSE and BIAS substantially higher; 18,013 km² and 168%, respectively). Supplementary Table 2 expands these results and includes statistics for these regions and other datasets included in ONFIRE, such as the USA, Europe, and Chile, where, in general, the global products tend to show systematic positive differences relative to the national references based on ONFIRE.

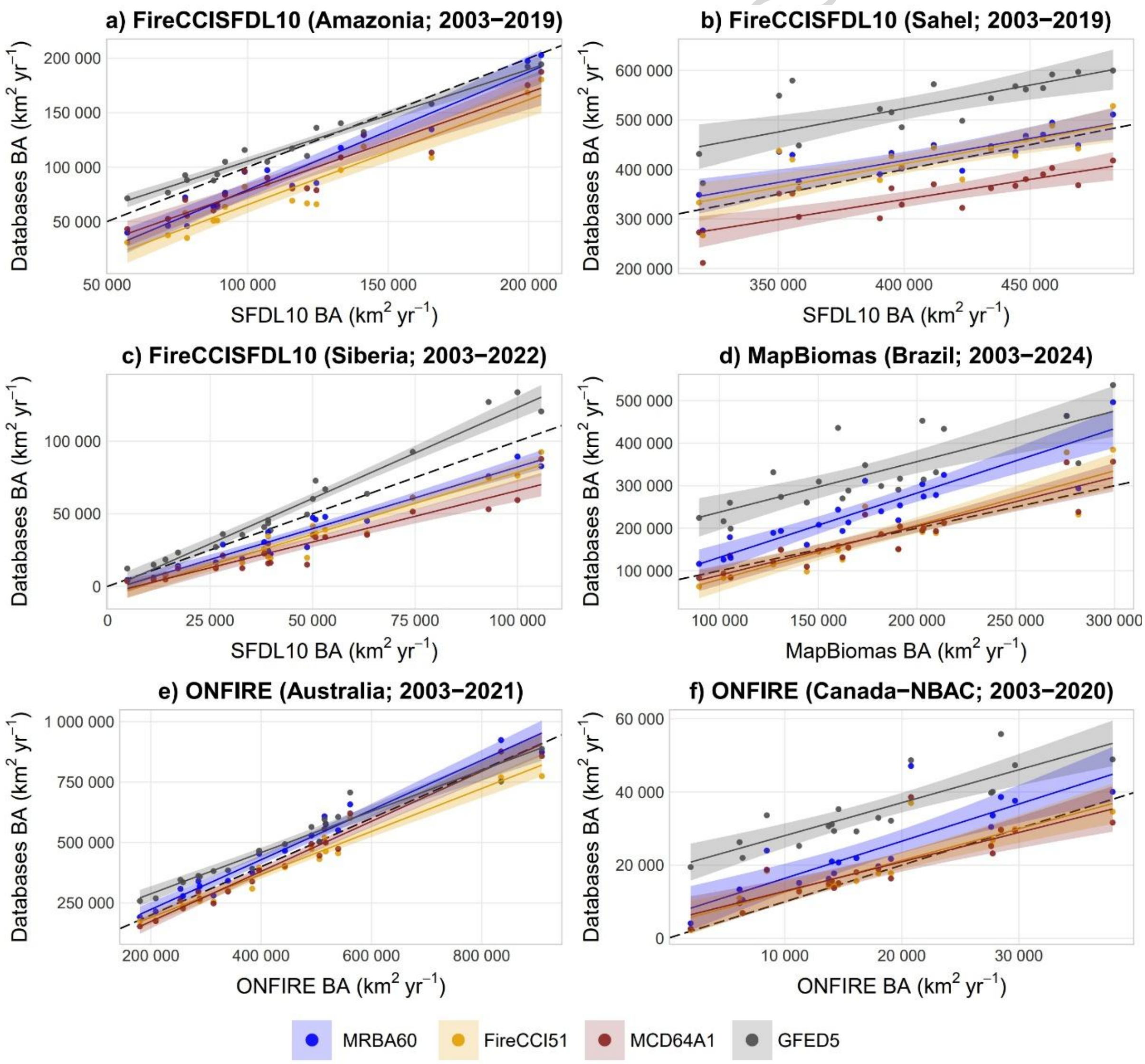

Figure 4. Regional validation of annual burned area sums of the global products (Y-axis) against independent reference datasets (X-axis) over the common periods available for each region: 2003-2019 in Amazonia and the Sahel, 2003-2020 in Canada, 2003-2022 in Siberia, 2003-2021 in Australia, and 2003-2024 in Brazil. Panels (a-c) compare the products with FireCCISFDL10 in Amazonia, Sahel, and Siberia; panel (d) with MapBiomas in Brazil; and panels (e-f) with ONFIRE in Australia and Canada (NBAC), respectively. Each point represents the annual BA ($km^2 \cdot year^{-1}$) of a product versus the corresponding reference; the black dashed line indicates the identity (1:1). The solid-coloured lines show the ordinary least squares linear fits, with their 95% confidence intervals shaded.

Figure 5 shows the spatial distribution of annual BA in Africa for 2016 and in Brazil for 2005. These cases are presented as illustrative examples of the available datasets. Africa is shown for 2016 because it is the only year of FireCCISFD11 available within the harmonised period for this region, while Brazil in 2005 is selected because FireCCI51 shows particularly pronounced edge artefacts in that year (see also Supplementary Figure 13 for a zoom on the edge artefact), which allows assessment of whether MRBA60 corrects it. In Africa, FireCCI51 estimates ~3.1 million km^2 (Mkm^2) burned, MRBA60 increases this figure to ~3.6 Mkm^2, and FireCCISFD11 reaches ~4.9 Mkm^2 (Figure 5a-c, respectively). MRBA60 shows less BA than FireCCISFD11 across much of the Sahel and south-central Africa, but more BA in the Congo Basin and other tropical rainforest regions (Figure 5d). Spatial consistency with FireCCISFD11 is high for both products, with Spearman correlation coefficients of 0.89 ($p < 0.05$) for FireCCI51 and 0.90 ($p < 0.05$) for MRBA60, indicating that the harmonisation applied in MRBA60 slightly improves the spatial agreement with FireCCISFD11, but does not fully reproduce its BA estimates. In Brazil in 2005 (Figure 5e-h), FireCCI51, MRBA60, and MapBiomas show similar patterns, with maxima localised in the Cerrado. However, comparison between MRBA60 and MapBiomas reveals that MRBA60 tends to systematically estimate more BA (~0.34 Mkm^2) than the national reference (~0.22 Mkm^2) across much of the territory, while the areas where MapBiomas exceeds MRBA60 are limited to specific regions. The Spearman correlation with respect to MapBiomas is 0.75 ($p < 0.05$) for FireCCI51 and 0.87 ($p < 0.05$) for MRBA60.

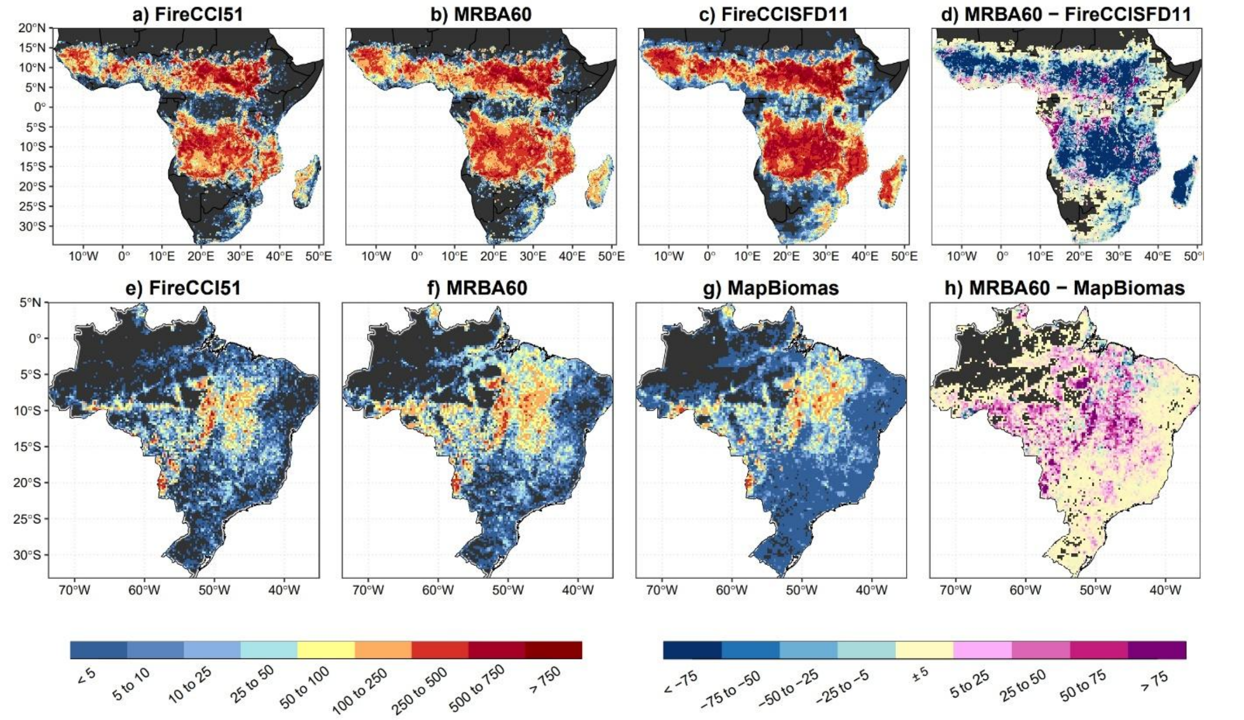

Figure 5. Spatial distribution of annual burned area in Africa (2016; panels a-d) and Brazil (2005; panels e-h). The BA maps (panels a-c, e-g) show the magnitude of annual burned area per grid cell (km²), while the difference panels (d, h) indicate overestimations (pink colours) and underestimations (blue colours) of MRBA60 relative to the reference products, also expressed in km². Black areas correspond to no-data regions.

Intercomparison with global products

Figure 6 shows the spatial pattern of mean annual BA according to MRBA60 (Figure 6a). The product reproduces the maxima of fire activity in the African savannas of both hemispheres, northern Australia, the north-central region of South America, northern India, and the Indo-Southeast Asian region. Activity is much lower in the subtropical deserts (Sahara, Arabian Peninsula, interior of Australia) and in most boreal and temperate humid regions, where BA is restricted to isolated hotspots. Figures 6b-d show differences in mean annual BA between MRBA60 and three reference products.

Compared with FireCCI51 (Figure 6b), MRBA60 tends to estimate more BA across extensive tropical areas, especially in the African savannas, regions of Tanzania and Mozambique, Madagascar, Central America, the Orinoco's Llanos and Amazonia, as well as in SE Asia (with a maximum in Myanmar), northern and eastern India, and north-eastern China. By contrast, it shows lower values in some regions, such as the humid Miombo and central Zambezi forests, and in the grasslands, savannas, and shrublands of South Sudan, northern Ivory Coast, and Ghana. This spatial pattern is consistent with the differences between FireCCI51 and FireCCIS311 in the training period (2019-2024), indicating that the harmonisation reasonably reproduces the characteristics of the reference product (see Supplementary Figure 14 for the mean differences between FireCCI51 and FireCCIS311 in 2019-2024).

Comparison with MCD64A1 (Figure 6c) reveals more pronounced differences in tropical and subtropical regions. MRBA60 shows systematically higher BA values across much of tropical Africa, in the northern and southern parts of the Asian subcontinent, and across extensive areas of central and southern America. In contrast, lower estimations are observed in areas close to Paraguay in the Southern Cone, in the grasslands, savannas, and shrublands of South Sudan, and in the deserts and xeric shrublands of the Kalahari and the interior of Australia. Finally, differences relative to GFED5 (Figure 6d) show a contrasting pattern. In general, MRBA60 estimates less BA than GFED5. However, areas with higher activity in MRBA60 are identified within the African savannas, the Orinoco's Llanos, parts of Amazonia (particularly in Cerrado mosaic landscapes), northern India, and arid regions of central Australia.

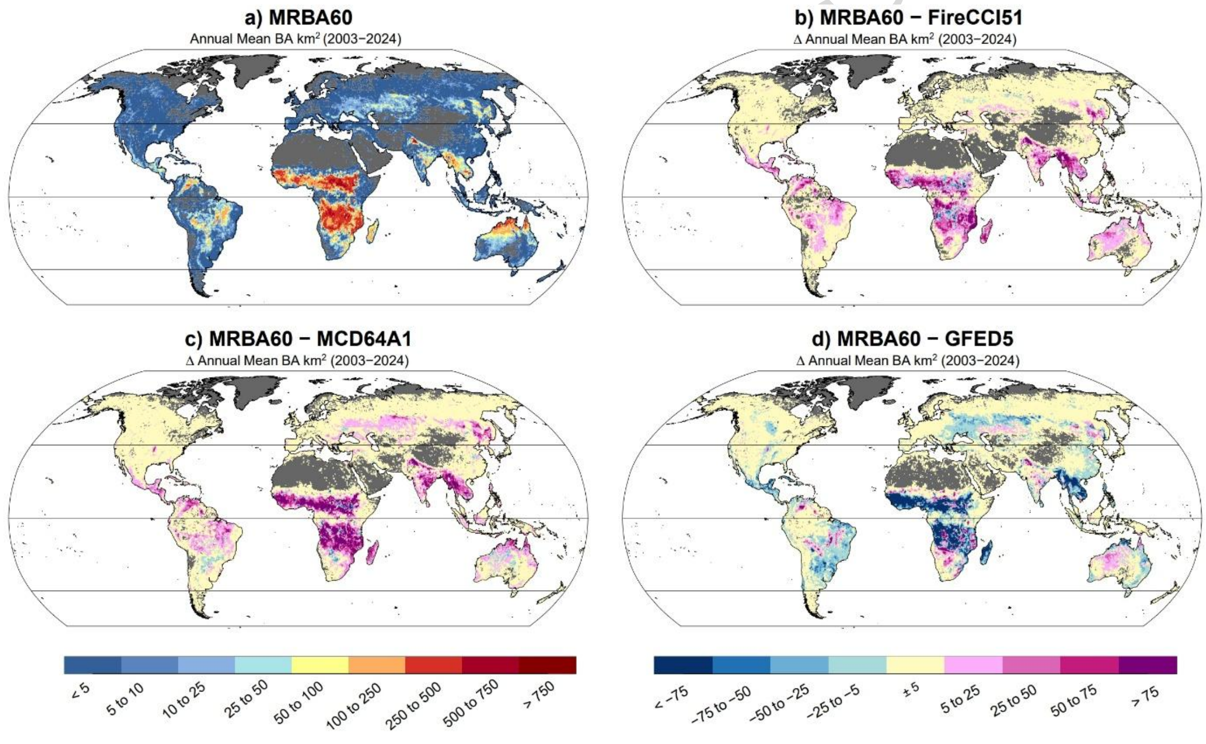

Figure 6. Mean annual burned area (BA) and product differences for 2003-2024. (a) Mean annual BA of MRBA60. (b-d) Difference in mean annual BA between MRBA60 and FireCCI51, MCD64A1, and GFED5, respectively. All values are expressed in km². In panels (b-d), pink colours indicate that MRBA60 reports more BA than the compared product, and blue colours indicate less BA (km²). Grey areas correspond to no-data regions.

Figure 7 shows the temporal evolution of global BA for the MRBA60, FireCCI51, MCD64A1, and GFED5 products at annual (Figure 7a) and seasonal (Figure 7b-e) scales. For the period 2003-2024, MRBA60 predicts a mean annual global BA of ~5.5 Mkm², compared with the ~4.4 Mkm² reported by FireCCI51. The grey bars represent the annual differences between MRBA60 and FireCCI51, which sum to ~24.5 Mkm² in 2003-2024, equivalent to ~1.1 Mkm² of additional BA per year (an increase of 25% relative to FireCCI51 over the same period). We compared BA trends by estimating Theil-Sen slopes[86] and assessing their significance using the modified Mann-Kendall test for autocorrelated data[87]. Trends are expressed as the accumulated change relative to the analysed period (%), calculated by normalising the estimated slope by the mean BA of the same period. Between 2003 and 2024, both FireCCI51 and MRBA60 showed declines in annual global BA, with accumulated relative changes of -33.3% and -25.1%, respectively. The other global reference products likewise confirm a reduction in BA. MCD64A1 shows an accumulated relative change of -30.1% (2003-2024), while GFED5 reports a decline of -21.7% (2003-2024), all of them statistically significant ($p < 0.05$).

We find that seasonal differences between MRBA60 and FireCCI51 are not uniform. The largest increase in BA in MRBA60 relative to FireCCI51 occurs in September-October-November (SON). Mean seasonal BA rises from 1.2 to 1.6 Mkm^2, and the accumulated difference reaches ~9.7 Mkm^2 over the 2003-2024 period. Next, MAM shows an increase from 0.5 Mkm^2 in FireCCI51 to 0.9 Mkm^2 in MRBA60, with ~8.3 Mkm^2 accumulated over the same period. In DJF, mean BA increases from 1.2 to 1.5 Mkm^2, totalling ~3.8 Mkm^2 over the same period. By contrast, the smallest increase is observed in June-July-August (JJA), where mean BA increases only from 1.5 to 1.6 Mkm^2, with ~2.5 Mkm^2 accumulated over 2003-2024. In general, seasonal differences between MRBA60 and FireCCI51 are positive, as MRBA60 estimates more BA than FireCCI51.

The temporal trends of BA estimated by the MRBA60 product for the whole period of analysis (2003-2024) indicate a reduction of fire occurrence in all seasons, with the strongest declines in SON (-33.1% in 2003-2024) and DJF (-25% in 2004-2024), and more moderate BA decreases in JJA (-23.4% in 2003-2024) and MAM (-6.8% in 2003-2024). Temporal trends of FireCCI51 show a broadly consistent seasonal signal, with particularly marked BA declines in SON (-47.2% in 2003-2024) and DJF (-33.7% in 2004-2024). Seasonal trends in the other global products confirm these patterns. MCD64A1 shows a pronounced decline in BA during SON (-37.1%), consistent with the decline observed in GFED5 (-30.9%). In GFED5, smaller BA declines are observed in DJF and JJA (-18.9% and -12.4%, respectively). All trends refer to the 2003-2024 period, except for DJF, which covers 2004-2024. In all cases, seasonal trends are statistically significant at the 95% confidence level ($p < 0.05$), except for MRBA60 in MAM.

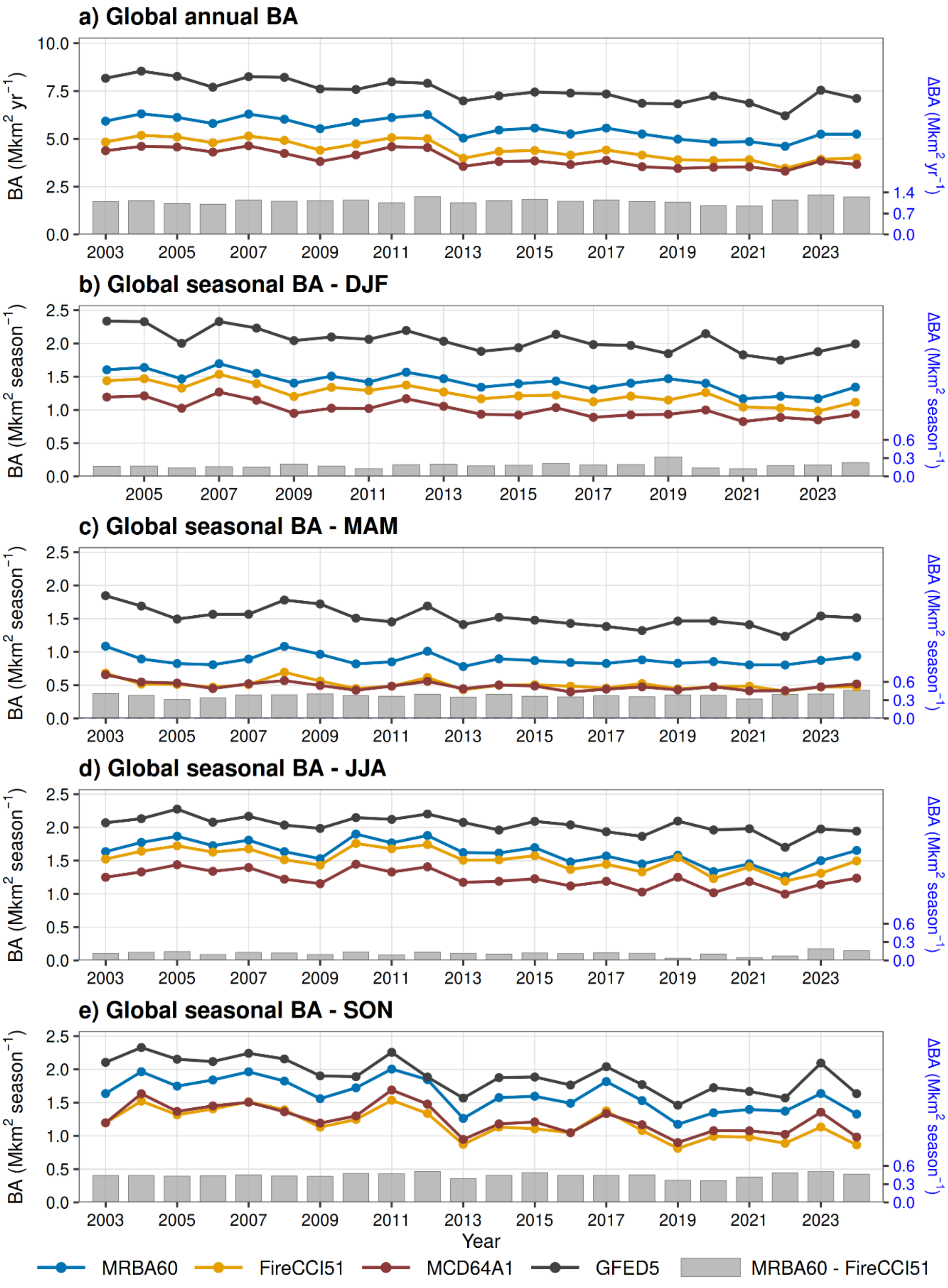

Figure 7. Temporal evolution of the global burned area (BA). Panel (a) shows the annual total BA for MRBA60 (blue; 2003-2024) and, for comparison, FireCCI51 (yellow; 2003-2024), MCD64A1

(green; 2003-2024), and GFED5 (grey; 2003-2024). Panels (b-e) show the corresponding seasonal totals for (b) DJF (December-January-February), (c) MAM (March-April-May), (d) JJA (June-July-August), and (e) SON (September-October-November). For DJF, the year 2003 is excluded because December 2002 is not available; the first complete DJF season is therefore DJF 2004. In all panels, the grey bars at the bottom represent the differences between MRBA60 and FireCCI51 for each year over their common period (2003-2024).

Finally, for each region[69] (see Supplementary Figure 5), we evaluated the regional monthly BA (mean 2003-2024) estimated by MRBA60, GFED5, and MCD64A1 (Figure 8; shown as lines) and the Spearman correlations between the products. Overall, the three products consistently reproduce the characteristic seasonal cycle of each region. Nevertheless, the largest deviations tend to coincide with months of moderate or low regional occurrence. At the region-month scale (14 regions × 12 months), MRBA60 predicted BA lies between GFED5 and MCD64A1 in 79.2% of cases.

In 10.1% of the combinations, MRBA60 estimates regional monthly BA values higher than GFED5, concentrated mainly in January-March and between May and November, with recurrences in a limited set of regions: Northern Hemisphere South America (NHSA; 3 months, cumulative difference of 12,393 km²), South-East Asia (SEAS; 2 months, 10,697 km²), Australia (AUST; 5 months, 12,934 km²), Central Asia (CEAS; June, 2,692 km²) and Equatorial Asia (EQAS; 4 months, 1,031 km²), Boreal North America (BONA; July, 26 km²) and Temperate North America (TENA; July, 11 km²); this represents ~0.72% of the global mean annual BA estimated by MRBA60 (~5.5 Mkm²). By contrast, in 10.7% of the combinations, MRBA60 estimates regional monthly climatological BA values that are lower than those from MCD64A1, mainly between January and May, with additional isolated cases in June, September and December, with recurrences in a limited set of regions: Southern Hemisphere South America (SHSA; 5 months, cumulative difference of 5,374 km²), Boreal Asia (BOAS; 2 months, 4,749 km²), Southern Africa (SHAF; April, 1,090 km²), Northern Hemisphere Africa (NHAF; September, 775 km²), the Middle East (MIDE; 5 months, 593 km²), South-East Asia (SEAS; September, 267 km²), Boreal North America (BONA; February-March, 62 km²) and Europe (EURO; June, 53 km²); in absolute terms, this corresponds to ~0.23% of the MRBA60 regional mean annual BA across the 14 GFED regions.

Regarding spatial consistency, the MRBA60 product shows higher agreement with GFED5 on average (mean Spearman correlation of 0.71; range 0.22 - 0.97) than with MCD64A1 (mean Spearman correlation of 0.65; range 0.10 - 0.94). Nevertheless, in 17.3% of the combinations, MRBA60 shows a slightly higher spatial correlation with MCD64A1 than with GFED5, for example, in the MIDE (during 12 months), CEAS during boreal summer (June-September), and BOAS in the winter and early spring months (December-March; period in which the model could not be fitted due to insufficient data and, consequently, MRBA60 mainly retains the FireCCI51 detections, see Supplementary Figure 2). In addition, correlation increases systematically with the magnitude of BA. The association between MRBA60 BA and correlation is very high (Spearman correlation ~0.92 for both comparisons), indicating that mean spatial patterns converge more clearly during months of higher fire activity. In all cases, correlations are statistically significant ($p < 0.05$).

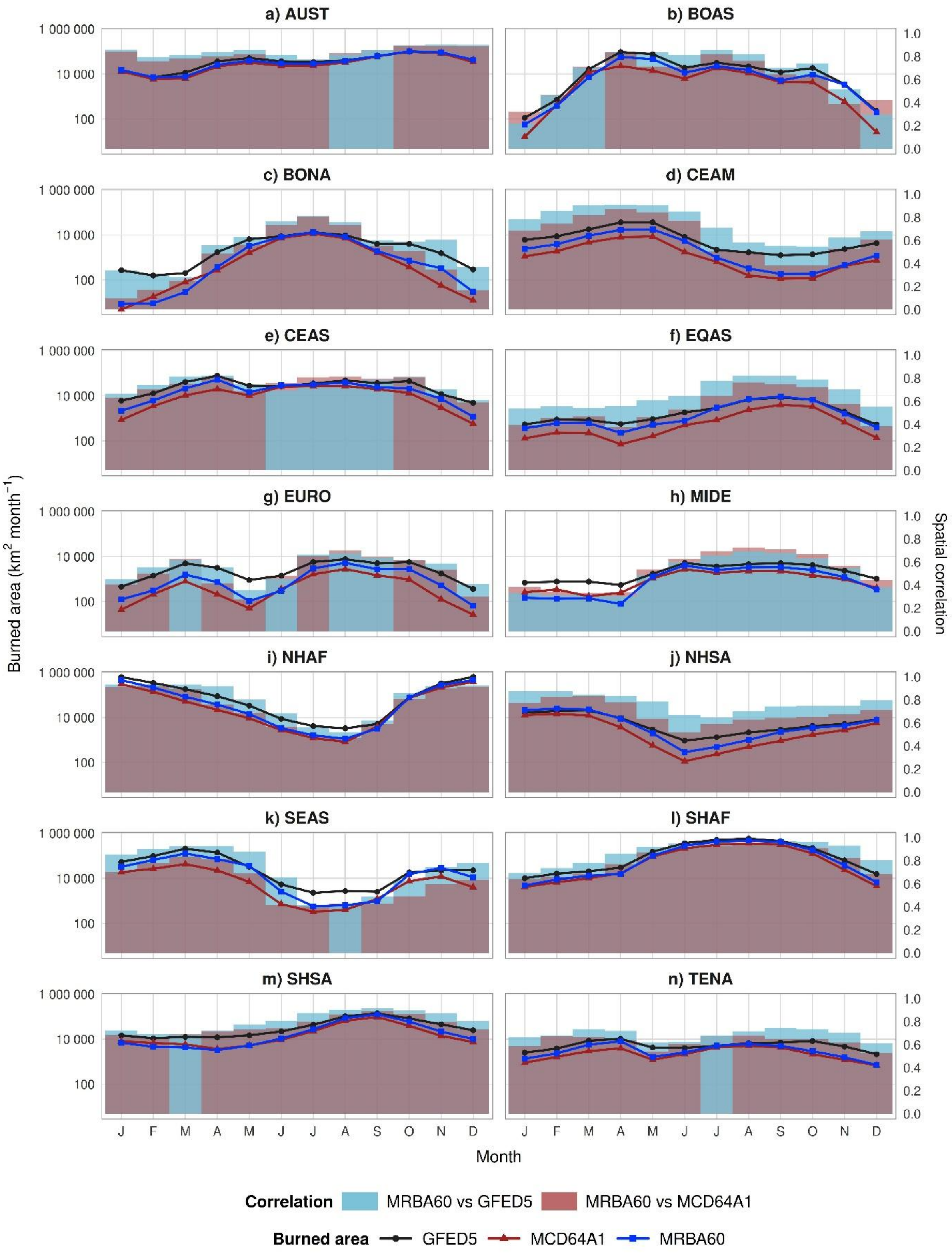
a) AUST
b) BOAS
c) BONA
d) CEAM
e) CEAS
f) EQAS
g) EURO
h) MIDE
i) NHAF
j) NHSA
k) SEAS
l) SHAF
m) SHSA
n) TENA
1 000 000
10 000
100
1.0
0.8
0.6
0.4
0.2
0.0
Burned area (km² month⁻¹)
Spatial correlation
J F M A M J J A S O N D
Month
Correlation MRBA60 vs GFED5 MRBA60 vs MCD64A1
Burned area GFED5 MCD64A1 MRBA60

Figure 8. Regional seasonality of burned area and spatial coherence across products (2003-2024). The lines show the regional integrated monthly burned area for MRBA60, GFED5, and MCD64A1 (left axis; logarithmic scale) across the 14 regions[69]. The shaded background shows the spatial Spearman correlation (right axis) between MRBA60 and GFED5 (blue) and between MRBA60 and MCD64A1 (burgundy), calculated within each region using the grid-cell-level monthly climatology (2003-2024 mean for each month).

Usage Notes

MRBA60 denotes the continuous global burned area (BA) time series from 2003 to the present, provided at 0.25° spatial resolution and monthly frequency. The series is obtained by temporally joining two CEDA-distributed BA products. For 2003-2018, MRBA60 uses the harmonised BA product MRBA60H[77], modelled following the procedures described in this paper and hosted at https://catalogue.ceda.ac.uk/uuid/db75c5f51ee240ae8743355dcebbb9b9/. From 2019 onwards, MRBA60 uses the 0.25° gridded FireCCIS311 product[24,27], hosted at https://catalogue.ceda.ac.uk/uuid/da8e669a74334c82a56e0b470bc4ef04/. Users should concatenate these two products temporally to obtain the complete MRBA60 series. FireCCIS311 also includes a separate 300 m pixel product, available at https://catalogue.ceda.ac.uk/uuid/d441079fc77f49fabeb41330612b252f/, but it is not part of the gridded MRBA60 time series described here. Annual updates of MRBA60 will be processed operationally under the Copernicus Climate Change Service (https://cds.climate.copernicus.eu/datasets/satellite-fire-burned-area).

MRBA60H was generated using a two-stage harmonisation scheme. First, biome- and month-specific Random Forest (RF) models were fitted, trained using FireCCIS311 as the reference product during the common period with FireCCI51 (2019-2024). Second, a bias correction using Quantile Mapping was applied to adjust the distribution of the harmonised BA. Therefore, MRBA60H should be understood as a historical series statistically aligned with FireCCIS311, not as an independent reconstruction of BA.

The continuous time series of MRBA60 for 2003 to the present, available at 0.25° spatial resolution and monthly frequency, is mainly intended for regional and global analyses requiring a monthly BA record that is temporally consistent and provided in a gridded format during the transition between MODIS-based FireCCI51 and Sentinel-3-based FireCCIS311. The product can be used for the evaluation of climate and Earth system models, fire-climate attribution studies, emission estimates, analyses of seasonal and interannual variability, and comparisons with other global BA products. By aligning the historical record with FireCCIS311, MRBA60 preserves the temporal coverage of FireCCI51 and leverages the detection improvements in the ESA current reference BA product. However, as it is distributed exclusively on a monthly 0.25° grid, the product implies a loss of detail compared with the pixel versions of the FireCCI51 and FireCCIS311 products, generated at spatial resolutions of 250 m and 300 m, respectively, as well as with regional datasets based on Landsat or Sentinel-2.

The validation and intercomparison presented in this study show improved agreement of MRBA60 with global reference datasets, independent Landsat data, high-resolution regional products, and national inventories. However, since FireCCIS311 is used as the target product in the harmonisation, MRBA60H may inherit part of its systematic biases, including possible omission and commission errors documented for the period 2019-2024[30].

The harmonisation models were calibrated using the maximum available overlap period between FireCCIS311 and the MODIS-based predictor series, that is, 2019-2024. Although this window currently represents the longest possible period, due to the availability of the Sentinel-3A/B constellation only after the launch and commissioning of Sentinel-3B in 2018, it remains relatively short for fully characterising fire climatology, interannual variability, and the main climate modes affecting fire activity. Consequently, the model mainly reflects the climate-fuel-fire relationships observed during the recent training period[9,16,88–90]. In addition, uncertainties in auxiliary predictors derived from reanalysis or satellite products may propagate into the harmonised estimates[76,91,92].

As is common in RF, predictions tend not to extrapolate beyond the range observed during training, which can compress the upper tail of the distribution and lead to underestimation of extreme values[54]. To avoid truncating historical extreme events outside the calibration range, the original FireCCI51 value was retained when it exceeded the regional and seasonal BAmax threshold. This rule affected only 0.13% of the monthly observations of burned grid cells, that is, 4,201 out of 3,327,921 monthly cells with BA > 0. This procedure is a conservative measure against the limited extrapolation capacity of RF, but should not be interpreted as a complete statistical extrapolation model. The auxiliary source mask allows these cases to be identified: class 1 corresponds to values harmonised using RF + QM, whereas class 2 identifies values retained from FireCCI51, enabling users to discard these grids in their analyses if needed.

MRBA60 should also be interpreted with caution while considering two important limitations related to spatial dependence and uncertainty. The evaluation against Landsat-derived TSA data, global datasets, and regional reference products provides an external and independent assessment of the product's performance, complementing the internal cell-level metrics. However, BA data are not spatially independent, as neighbouring cells may share climatic conditions, fuel availability, fire-regime characteristics, and detection errors. No spatial blocking was applied when deriving the internal cell-level validation metrics. Although the modelling framework is structured by biome and month, it includes latitude and longitude as spatial predictors, and restricts harmonisation to cells included in the fire mask; values and residuals from nearby cells should not be considered fully independent. Consequently, the internal cell-level metrics should be understood as a first-order approximation of model performance rather than as a complete characterisation of spatially independent errors. In addition, the uncertainty variable has a different interpretation before and after 2019. For 2003-2018, it represents an empirical first-order approximation based on the RMSE of the MRBA60H harmonisation error, whereas from 2019 onwards it corresponds to the standard error provided by FireCCIS311. Although both estimates are expressed in m^2, they are derived from different methods and should not be treated as a single homogeneous uncertainty time series.

Overall, users should consider these limitations when interpreting MRBA60. These considerations could be particularly relevant for studies focused on regional extremes, trend attribution, or uncertainty propagation. Whenever possible, results obtained with MRBA60 should be compared with independent references, such as Landsat perimeters, national or regional inventories, and other BA products.

Data availability

The MRBA60H version 6.0 dataset is archived at the Centre for Environmental Data Analysis (CEDA) as a versioned collection of NetCDF files (https://catalogue.ceda.ac.uk/uuid/db75c5f51ee240ae8743355dcebbb9b9/). The 0.25° aggregated raster files derived from Landsat burned-area perimeters (TSA), generated for validation over the period 2017-2024, are available at Zenodo (https://doi.org/10.5281/zenodo.20345350). In addition, the monthly harmonisation mask indicating the grid cells where harmonisation was applied and where the original FireCCI51 values were retained is available at Zenodo (https://doi.org/10.5281/zenodo.20347202).

Code availability

The complete processing and validation workflow used to generate the MRBA60H dataset has been archived as an immutable versioned record in Zenodo (DOI: 10.5281/zenodo.20698934)[93]. The archived repository contains the exact code version used to generate the dataset, together with information on the computational environment, software dependencies, directory structure, and reproducibility examples. The code was primarily developed in R and executed in a high-performance computing (HPC) environment using monthly global gridded datasets at 0.25° spatial resolution for the 2003-2024 period.

Acknowledgements

This research was funded under the European Space Agency (ESA) Climate Change Initiative (CCI) project FireCCI, contract number 4000126706/19/I-NB.

Author contributions

Miguel Ángel Torres-Vázquez (MAT-V) designed the methodology, processed and harmonised the burned area data, performed the statistical analyses, prepared the data, figures, and tables, and led the writing of the manuscript. Carlota Segura-Garcia (CS-G) contributed to methodological discussions, data analysis, and the writing and revision of the manuscript. Marco Turco (MT) contributed to the methodological design and to the writing and revision of the manuscript. Amin Khairoun (AK), M. Lucrecia Pettinari (MLP), Erika Solano-Romero (ES-R), Mariano García (MG), Patricia Oliva (PO), and Matthew W. Jones (MWJ) contributed to methodological discussions, interpretation of results, writing, and revision of the manuscript. Emilio Chuvieco (EC) conceived the study, supervised the work, secured funding, and contributed to the writing and revision of the manuscript.

Funding

MAT-V, AK, and MLP have received funding from the European Space Agency (ESA) through the FireCCI project, contract number 4000126706/19/I-NB.

Competing interests

The authors declare no competing interests.

References

1. Bowman, D. M. J. S. *et al.* Wildfires: Australia needs national monitoring agency. *Nature* **584**, 188–191 (2020).
2. Jones, M. W. *et al.* Global and regional trends and drivers of fire under climate change. *Rev. Geophys.* **60**, e2020RG000726 (2022).
3. Pausas, J. G. & Keeley, J. E. Wildfires as an ecosystem service. *Front. Ecol. Environ.* **17**, 289–295 (2019).
4. Jolly, W. M. *et al.* Climate-induced variations in global wildfire danger from 1979 to 2013. *Nat. Commun.* **6**, 7537 (2015).
5. Bowman, D. M. J. S. *et al.* Human exposure and sensitivity to globally extreme wildfire events. *Nat. Ecol. Evol.* **1**, 58 (2017).
6. Abatzoglou, J. T., Williams, A. P., Boschetti, L., Zubkova, M. & Kolden, C. A. Global patterns of interannual climate–fire relationships. *Glob. Change Biol.* **24**, 5164–5175 (2018).
7. Jones, M. W. *et al.* State of wildfires 2023-2024. *Earth Syst. Sci. Data* **16**, 3601–3685 (2024).
8. Cunningham, C. X. *et al.* Climate-linked escalation of societally disastrous wildfires. *Science* **390**, 53–58 (2025).
9. Kelley, D. I. *et al.* State of Wildfires 2024-2025. *Earth Syst. Sci. Data* **17**, 5377–5488 (2025).
10. Teymoor Seydi, S. *et al.* Increasing global human exposure to wildland fires despite declining burned area. *Science* **389**, 826–829 (2025).
11. Chen, Y., Morton, D. C., Andela, N., Giglio, L. & Randerson, J. T. How much global burned area can be forecast on seasonal time scales using sea surface temperatures? *Environ. Res. Lett.* **11**, 045001 (2016).
12. Turco, M. *et al.* Skilful forecasting of global fire activity using seasonal climate predictions. *Nat. Commun.* **9**, 2718 (2018).
13. Torres-Vázquez, M. Á. *et al.* Enhancing seasonal fire predictions with hybrid dynamical and random forest models. *Npj Nat. Hazards* **2**, 20 (2025).
14. Pereira, J., Mendes, J., Júnior, J. S. S., Viegas, C. & Paulo, J. R. A review of genetic algorithm approaches for wildfire spread prediction calibration. *Mathematics* **10**, 300 (2022).
15. McFarland, J. R. Extreme fire spread events burn more severely and homogenize postfire landscapes in the southwestern United States. *Glob. Change Biol.* **31**, e70106 (2025).

16. Andela, N. *et al.* A human-driven decline in global burned area. *Science* **356**, 1356–1362 (2017).
17. Chuvieco, E. *et al.* Human and climate drivers of global biomass burning variability. *Sci. Total Environ.* **779**, 146361 (2021).
18. García, M. *et al.* Characterizing global fire regimes from satellite-derived products. *Forests* **13**, 699 (2022).
19. Gincheva, A. *et al.* The interannual variability of global burned area is mostly explained by climatic drivers. *Earth's Future* **12**, e2023EF004334 (2024).
20. Alonso-Canas, I. & Chuvieco, E. Global burned area mapping from ENVISAT-MERIS and MODIS active fire data. *Remote Sens. Environ.* **163**, 140–152 (2015).
21. Chuvieco, E. *et al.* A new global burned area product for climate assessment of fire impacts. *Glob. Ecol. Biogeogr.* **25**, 619–629 (2016).
22. Chuvieco, E. *et al.* Generation and analysis of a new global burned area product based on MODIS 250 m reflectance bands and thermal anomalies. *Earth Syst. Sci. Data* **10**, 2015–2031 (2018).
23. Lizundia-Loiola, J., Otón, G., Ramo, R. & Chuvieco, E. A spatio-temporal active-fire clustering approach for global burned area mapping at 250 m from MODIS data. *Remote Sens. Environ.* **236**, 111493 (2020).
24. Lizundia-Loiola, J., Franquesa, M., Khairoun, A. & Chuvieco, E. Global burned area mapping from Sentinel-3 Synergy and VIIRS active fires. *Remote Sens. Environ.* **282**, 113298 (2022).
25. Henocq, C. *et al.* OLCI/SLSTR SYN L2 algorithm and products overview. in 8723–8726 (IEEE, Valencia, Spain, 2018). doi:10.1109/IGARSS.2018.8517420.
26. Schroeder, W., Oliva, P., Giglio, L. & Csiszar, I. A. The new VIIRS 375 m active fire detection data product: Algorithm description and initial assessment. *Remote Sens. Environ.* **143**, 85–96 (2014).
27. Khairoun, A. *et al. ESA CCI ECV Fire Disturbance: D2.2 Algorithm Theoretical Basis Document (ATBD) - SYN*. https://climate.esa.int/media/documents/Fire_cci_D2.2_ATBD-SYN_v1.1.pdf (2023).
28. Franquesa, M. *et al.* Development of a standard database of reference sites for validating global burned-area products. *Earth Syst. Sci. Data* **12**, 3229–3246 (2020).
29. Franquesa, M., Lizundia-Loiola, J., Stehman, S. V. & Chuvieco, E. Using long temporal reference units to assess the spatial accuracy of global satellite-derived burned area products. *Remote Sens. Environ.* **269**, 112823 (2022).
30. Stroppiana, D. *et al. ESA CCI ECV Fire Disturbance: D4.1 Product Validation and Intercomparison Report*. https://climate.esa.int/documents/3064/Fire_cci_D4.1_PVIR_v3.0.pdf (2024).
31. Global Climate Observing System. *The 2022 GCOS Implementation Plan*. https://library.wmo.int/idurl/4/58104 (2022).
32. Global Climate Observing System. *The 2022 GCOS ECVs Requirements*. https://library.wmo.int/idurl/4/58111 (2022).
33. Fernández-García, V. & Kull, C. A. Refining historical burned area data from satellite observations. *Int. J. Appl. Earth Obs. Geoinformation* **120**, 103350 (2023).

34. Guo, Z. *et al.* Reconstructed global monthly burned area maps from 1901 to 2020. *Earth Syst. Sci. Data* **17**, 3599–3618 (2025).

35. Chuvieco, E., Pettinari, M. L., Lizundia-Loiola, J. & Franquesa, M. ESA Fire Climate Change Initiative (Fire_cci): MODIS Fire_cci Burned Area GRID Product, Version 5.1 (2023-2024). Zenodo https://doi.org/10.5281/zenodo.20346362 (2026).

36. Giglio, L., Schroeder, W. & Justice, C. O. The Collection 6 MODIS active fire detection algorithm and fire products. *Remote Sens. Environ.* **178**, 31–41 (2016).

37. Hersbach, H. *et al.* The ERA5 global reanalysis. *Q. J. R. Meteorol. Soc.* **146**, 1999–2049 (2020).

38. Soci, C. The ERA5 global reanalysis from 1940 to 2022. *Q. J. R. Meteorol. Soc.* **150**, 4014–4048 (2024).

39. Abatzoglou, J. T., Dobrowski, S. Z., Parks, S. A. & Hegewisch, K. C. TerraClimate, a high-resolution global dataset of monthly climate and climatic water balance from 1958–2015. *Sci. Data* **5**, 170191 (2018).

40. Miralles, D. G. *et al.* GLEAM4: Global land evaporation and soil moisture dataset at 0.1° resolution from 1980 to near present. *Sci. Data* **12**, 416 (2025).

41. Vitolo, C. *et al.* ERA5-based global meteorological wildfire danger maps. *Sci. Data* **7**, 216 (2020).

42. Didan, K. MODIS/Terra Vegetation Indices Monthly L3 Global 0.05Deg CMG V061. NASA Land Processes Distributed Active Archive Center https://doi.org/10.5067/MODIS/MOD13C2.061 (2021).

43. Chen, Y. *et al.* Multi-decadal trends and variability in burned area from the fifth version of the Global Fire Emissions Database (GFED5). *Earth Syst. Sci. Data* **15**, 5227–5259 (2023).

44. Fick, S. E. & Hijmans, R. J. WorldClim 2: New 1-km spatial resolution climate surfaces for global land areas. *Int. J. Climatol.* **37**, 4302–4315 (2017).

45. Harris, I., Osborn, T. J., Jones, P. & Lister, D. Version 4 of the CRU TS monthly high-resolution gridded multivariate climate dataset. *Sci. Data* **7**, 109 (2020).

46. Kobayashi, S. *et al.* The JRA-55 reanalysis: General specifications and basic characteristics. *J. Meteorol. Soc. Jpn. Ser II* **93**, 5–48 (2015).

47. Van Wagner, C. E. *Development and Structure of the Canadian Forest Fire Weather Index System*. (1987).

48. Abatzoglou, J. T., Williams, A. P. & Barbero, R. Global emergence of anthropogenic climate change in fire weather indices. *Geophys. Res. Lett.* **46**, 326–336 (2019).

49. Matteo, A. *et al.* Challenges in assessing fire weather changes in a warming climate. *Npj Clim. Atmospheric Sci.* **8**, 284 (2025).

50. Quilcaille, Y., Batibeniz, F., Ribeiro, A. F. S., Padrón, R. S. & Seneviratne, S. I. Fire weather index data under historical and shared socioeconomic pathway projections in the 6th phase of the Coupled Model Intercomparison Project from 1850 to 2100. *Earth Syst. Sci. Data* **15**, 2153–2177 (2023).

51. SantanderMetGroup. ATLAS/reference-grids at main · SantanderMetGroup/ATLAS. https://github.com/SantanderMetGroup/ATLAS/tree/main/reference-grids.

52. Illarionova, S. Exploration of geo-spatial data and machine learning algorithms for robust wildfire occurrence prediction. *Sci. Rep.* **15**, 10712 (2025).

53. Yu, Y. *et al.* Quantifying the drivers and predictability of seasonal changes in African fire. *Nat. Commun.* **11**, 2893 (2020).
54. Breiman, L. Random forests. *Mach. Learn.* **45**, 5–32 (2001).
55. Dinerstein, E. *et al.* An ecoregion-based approach to protecting half the terrestrial realm. *BioScience* **67**, 534–545 (2017).
56. Mason, S. J. & Graham, N. E. Conditional probabilities, relative operating characteristics, and relative operating levels. *Weather Forecast.* **14**, 713–725 (1999).
57. Mason, S. J. & Graham, N. E. Areas beneath the relative operating characteristics (ROC) and relative operating levels (ROL) curves: Statistical significance and interpretation. *Q. J. R. Meteorol. Soc.* **128**, 2145–2166 (2002).
58. Fluss, R., Faraggi, D. & Reiser, B. Estimation of the Youden Index and its associated cutoff point. *Biom. J.* **47**, 458–472 (2005).
59. Benjamini, Y. & Hochberg, Y. Controlling the false discovery rate: A practical and powerful approach to multiple testing. *J. R. Stat. Soc. Ser. B Methodol.* **57**, 289–300 (1995).
60. Ventura, V., Paciorek, C. J. & Risbey, J. S. Controlling the proportion of falsely rejected hypotheses when conducting multiple tests with climatological data. *J. Clim.* **17**, 4343–4356 (2004).
61. Dormann, C. F. *et al.* Collinearity: A review of methods to deal with it and a simulation study evaluating their performance. *Ecography* **36**, 27–46 (2013).
62. Liaw, A. & Wiener, M. Classification and regression by randomForest. *R News* **2**, 18–22 (2002).
63. Kuhn, M. *et al.* caret: Classification and Regression Training. Comprehensive R Archive Network https://doi.org/10.32614/CRAN.package.caret (2024).
64. Greenwell, B. fastshap: Fast Approximate Shapley Values. Comprehensive R Archive Network https://doi.org/10.32614/CRAN.package.fastshap (2024).
65. Panofsky, H. A. & Brier, G. W. *Some Applications of Statistics to Meteorology*. (Earth and Mineral Sciences Continuing Education, College of Earth and Mineral Sciences, The Pennsylvania State University, University Park, Pennsylvania, 1968).
66. Bedia, J., Herrera, S., Camia, A., Moreno, J. M. & Gutiérrez, J. M. Seasonal predictions of Fire Weather Index: Paving the way for their operational applicability in Mediterranean Europe. *Clim. Serv.* **9**, 101–110 (2018).
67. Gudmundsson, L., Bremnes, J. B., Haugen, J. E. & Engen-Skaugen, T. Technical Note: Downscaling RCM precipitation to the station scale using statistical transformations: A comparison of methods. *Hydrol. Earth Syst. Sci.* **16**, 3383–3390 (2012).
68. Snyder, J. P. *Map Projections: A Working Manual*. 385 https://doi.org/10.3133/pp1395 (1987) doi:10.3133/pp1395.
69. Giglio, L., van der Werf, G. R., Randerson, J. T., Collatz, G. J. & Kasibhatla, P. Global estimation of burned area using MODIS active fire observations. *Atmospheric Chem. Phys.* **6**, 957–974 (2006).
70. van der Werf, G. R. Landscape fire emissions from the fifth version of the Global Fire Emissions Database (GFED5). *Sci. Data* **12**, 1870 (2025).
71. Chen, Y. Tracking recent extremes and interannual variability of global fire emissions using a near-real-time extension to the Global Fire Emissions Database. *Earth Syst. Sci. Data Discuss.* (2026).

72. Giglio, L., Boschetti, L., Roy, D. P., Humber, M. L. & Justice, C. O. The Collection 6 MODIS burned area mapping algorithm and product. *Remote Sens. Environ.* **217**, 72–85 (2018).
73. Giglio, L., Justice, C., Boschetti, L. & Roy, D. MODIS/Terra+Aqua Burned Area Monthly L3 Global 500m SIN Grid V061. NASA Land Processes Distributed Active Archive Center https://doi.org/10.5067/MODIS/MCD64A1.061 (2021).
74. Silveira, E. M. O. *et al.* Nationwide native forest structure maps for Argentina based on forest inventory data, SAR Sentinel-1 and vegetation metrics from Sentinel-2 imagery. *Remote Sens. Environ.* **285**, 113391 (2023).
75. Khairoun, A. *et al. ESA CCI ECV Fire Disturbance: D2.2 End to End ECV Uncertainty Budget, Version 2.1*. https://climate.esa.int/en/projects/fire/key-documents/ (2021).
76. Brennan, J., Gómez-Dans, J. L., Disney, M. & Lewis, P. Theoretical uncertainties for global satellite-derived burned area estimates. *Biogeosciences* **16**, 3147–3164 (2019).
77. Chuvieco, E., Pettinari, M. L. & Torres-Vázquez, M. Á. ESA Fire Climate Change Initiative (FireCCI): Harmonised Medium Resolution Burned Area Grid product, version 6.0 (MRBA60H). NERC EDS Centre for Environmental Data Analysis https://doi.org/10.5285/db75c5f51ee240ae8743355dcebbb9b9 (2026).
78. Torres-Vázquez, M. Á. Monthly Harmonisation Mask (MRBA60). Zenodo https://doi.org/10.5281/zenodo.20347202 (2026).
79. Torres-Vázquez, M. Á. & Solano-Romero, E. Annual Rasterized BARD Burned Area Reference Data for MRBA60 Validation. Zenodo https://doi.org/10.5281/zenodo.20345350 (2026).
80. Khairoun, A. & Solano, E. *ESA CCI ECV Fire Disturbance: D2.2.2 Algorithm Theoretical Basis Document (ATBD) - Small Fires Dataset Long Term (SFDL)*. https://climate.esa.int/documents/2796/Fire_cci_D2.2.2_ATBD_SFDL_v1.2.pdf (2023).
81. Khairoun, A. Peat fires contribute disproportionately to Siberian fire carbon emissions. *Sci. Adv.* **12**, eadl2368 (2026).
82. Gincheva, A. A monthly gridded burned area database of national wildland fire data. *Sci. Data* **11**, 352 (2024).
83. Gincheva, A. & Turco, M. ONFIRE Dataset: Monthly Gridded Burned Area data. Zenodo https://doi.org/10.5281/zenodo.8289245 (2023).
84. Alencar, A. A. C. *Algorithm Theoretical Basis Document (ATBD) - MapBiomas Fire Collection 4*. https://brasil.mapbiomas.org/wp-content/uploads/sites/4/2025/06/ATBD-MapBiomas-Fogo-Colecao-4.pdf (2024).
85. Roteta, E., Bastarrika, A., Padilla, M., Storm, T. & Chuvieco, E. Development of a Sentinel-2 burned area algorithm: Generation of a small fire database for sub-Saharan Africa. *Remote Sens. Environ.* **222**, 1–17 (2019).
86. Sen, P. K. Estimates of the regression coefficient based on Kendall's tau. *J. Am. Stat. Assoc.* **63**, 1379–1389 (1968).
87. Hamed, K. H. & Rao, A. R. A modified Mann-Kendall trend test for autocorrelated data. *J. Hydrol.* **204**, 182–196 (1998).
88. Jain, P., Castellanos-Acuna, D., Coogan, S. C. P., Abatzoglou, J. T. & Flannigan, M. D. Observed increases in extreme fire weather driven by atmospheric humidity and temperature. *Nat. Clim. Change* **12**, 63–70 (2022).

89. Jones, M. W. *et al.* Global rise in forest fire emissions linked to climate change in the extratropics. *Science* **386**, eadl5889 (2024).
90. Abatzoglou, J. T. *et al.* Climate change has increased the odds of extreme regional forest fire years globally. *Nat. Commun.* **16**, 6390 (2025).
91. Sun, Q. *et al.* A review of global precipitation data sets: Data sources, estimation, and intercomparisons. *Rev. Geophys.* **56**, 79–107 (2018).
92. Duveiller, G. Getting the leaves right matters for estimating temperature extremes. *Geosci. Model Dev.* **16**, 7357–7373 (2023).
93. Torres-Vázquez, M. Á. Supplementary Code Torres-Vázquez et al. (2026): Harmonised Medium Resolution Burned Area product. Zenodo https://doi.org/10.5281/zenodo.20698934 (2026).